On the Mechanisms Driving Latent Heat Flux Variations in the Northwest Tropical Atlantic: a Modeling Approach

Pablo Fernández[1], Sabrina Speich[2], Carlos Conejero[3,4], Lionel Renault[3], Fabien Desbiolles[3], Claudia Pasquero[5], and Guillaume Lapeyre[2]

[1]Laboratoire d'Océanographie et du Climat: Expérimentations et Approches Numériques, Sorbonne Université, Paris, France.
[2]Laboratoire de Météorologie Dynamique, École Normale Supérieure, Department of Geosciences, Paris, France.
[3]LEGOS, University of Toulouse, IRD, CNRS, CNES, UPS, Toulouse, France
[4]ENTROPIE (IRD, CNRS, Ifremer, Université de la Réunion, Université de la Nouvelle-Calédonie), Nouméa, New Caledonia.
[5]Department of Earth and Environmental Sciences, University of Milano - Bicocca, Milan, Italy.

Correspondence: Pablo Fernández (pablo.fernandez-fernandez@locean.ipsl.fr)

Abstract. In this study, a high-resolution ocean-atmosphere coupled simulation is used to assess the effects of sea surface temperature (SST), surface currents, and ocean vertical stratification on the spatial variability of latent heat flux (LHF) and the stability of the marine atmospheric boundary layer (MABL) in the Northwest Tropical Atlantic during January and February 2020. The analysis focuses on the ocean mesoscale ($O(50-250$ km$)$) across the Northwest Tropical Atlantic (referred to as

5   the EURECA region in this study) and within three sub-regions characterized by different ocean dynamical regimes: Amazon, Downstream, and Tradewind. Results indicate that the coupling between SST and wind speed (and specific humidity) is stronger (weaker) in the Amazon and Downstream regions (influenced by the warm coastal North Brazil Current eddy corridor and the Amazon river plume) than in the Tradewind region (representative of the open ocean), consistent with previous remote sensing studies. Overall, warmer SSTs are associated with increased wind speeds and variations in specific humidity, deviating

10   from Clausius-Clapeyron expectations. We interpret this as the result of active ocean processes modifying the near-surface atmosphere, enhancing vertical motion in the MABL, and transporting momentum and drier air from the free troposphere toward the surface. This effect is particularly pronounced over waters influenced by the Amazon plume, where positive SST anomalies persist, primarily due to lateral advection in the mixed layer. To further investigate the impact of mesoscale SST features on LHF, we apply a linear, SST-based downscaling method. Results show that these mesoscale SST structures induce

15   a substantial increase in LHF, 46.8 W m^{-2} K^{-1} on average in the Amazon and Downstream regions (warm eddy corridor). In the Tradewind region, the LHF sensitivity to SST is smaller, at about 35 W m^{-2} K^{-1}. For the Amazon region, of the 46.7 W m^{-2} K^{-1} change in LHF associated with SST, approximately 7.8 W m^{-2} K^{-1} is attributed to direct mesoscale SST changes (thermodynamic contribution), while the remainder is linked to mesoscale SST-induced modifications in near-surface atmospheric circulation (dynamic contribution). Within the dynamic contribution, about 80% (31.1 W m^{-2} K^{-1} out

20   of 38.9 W m^{-2} K^{-1}) is due to variations in specific humidity undersaturation, and the remaining 20% (7.8 W m^{-2} K^{-1} out of 38.9 W m^{-2} K^{-1}) is due to wind speed changes. Similar relative contributions are found in the other subregions and in the overall EURECA domain. Finally, the influence of surface currents on winds is weaker, with LHF deviations not exceeding

15 W m^{-2}. This study underscores the importance of a regionalized approach to mesoscale air-sea interaction studies in the Northwest Tropical Atlantic, as LHF sensitivity to SST and surface currents exhibits strong spatial variability driven by distinct oceanic dynamics. Submesoscale LHF sensitivity to SST and currents is not addressed here and will be the subject of future research.

1 Introduction

Turbulent heat fluxes (THFs) are related to temperature (sensible) and moisture undersaturation (latent) imbalances at the air-sea interface. When examining air-sea interactions through THFs, it is common in the literature to distinguish between the ocean's large-scale and *fine-scale* processes, which include the mesoscale ($O(50-250$ km$)$) and submesoscale ($< O(50$ km$)$) components. These *fine-scale* interactions with the atmosphere have been shown to differ significantly from large-scale processes (Chelton and Xie, 2010; Small et al., 2019; Gentemann et al., 2020; Conejero et al., 2024). At large scales, atmospheric dynamics predominantly drive ocean variability (Gill and Adrian, 1982). However, at scales smaller than 250 km, the ocean actively influences the near-surface atmosphere, affecting air temperature, frictional stress, and the stability of the marine atmospheric boundary layer (MABL) (Small et al., 2008). Among THFs, this study focuses on latent heat flux (LHF) in the Northwest Tropical Atlantic, as it provides a direct link between atmospheric dynamics and thermodynamics.

The effects of *fine-scale* sea-surface temperature (SST) variability on the near-surface atmosphere and air-sea heat fluxes, particularly LHF, have been investigated using satellite products (Bishop et al., 2017; Fernández et al., 2023), *in-situ* measurements (Acquistapace et al., 2022; Iyer et al., 2022; Fernández et al., 2024), and atmospheric models (Borgnino et al., 2025). In the literature, two primary mechanisms of lower atmospheric response to SST features have been identified: the downward momentum mixing (DMM) (Hayes et al., 1989; Wallace et al., 1989) and the pressure adjustment (PA) (Lindzen and Nigam, 1987). In the DMM mechanism (Fig. 1a), a warm SST anomaly destabilizes the MABL, enhancing vertical mixing. This process facilitates the entrainment of drier air from the free troposphere into the MABL, thereby increasing surface winds and intensifying LHF (Acquistapace et al., 2022; Borgnino et al., 2025). Conversely, cold SST anomalies suppress vertical mixing, leading to reduced surface winds and lower LHF. Thus, DMM provides a *top-down* mechanism by which *fine-scale* SST variability influences the near-surface atmosphere, a process known as thermal feedback (TFB) (Renault et al., 2019b, 2023). PA, on the other hand, predicts that surface wind convergence (divergence) occurs over SST maxima (minima) as warm (cold) SST cores generate local sea level pressure lows (highs). This leads to weaker winds over SST extrema, resulting in lower LHF (Pasquero et al., 2021). The influence of these mechanisms has been observed across various regions of the World Ocean on timescales ranging from hours to weeks. Foussard et al. (2019) found that PA tends to dominate where surface winds are well-coupled to upper-level winds, while DMM prevails in neutrally stable lower tropospheric conditions where SST effectively modulates surface winds (Desbiolles et al., 2023). Warm mesoscale eddies have been shown to enhance LHF via DMM in several regions, including the Gulf Stream (Minobe et al., 2008), the Kuroshio Extension (Xu et al., 2011; Ma et al., 2015; Chen et al., 2017), the South China Sea (Liu et al., 2018, 2020), and the Agulhas (O'Neill et al., 2005) and Malvinas (Villas Bôas et al., 2015; Leyba et al., 2017) currents. Meanwhile, PA has been shown to impact cloud and precipitation patterns
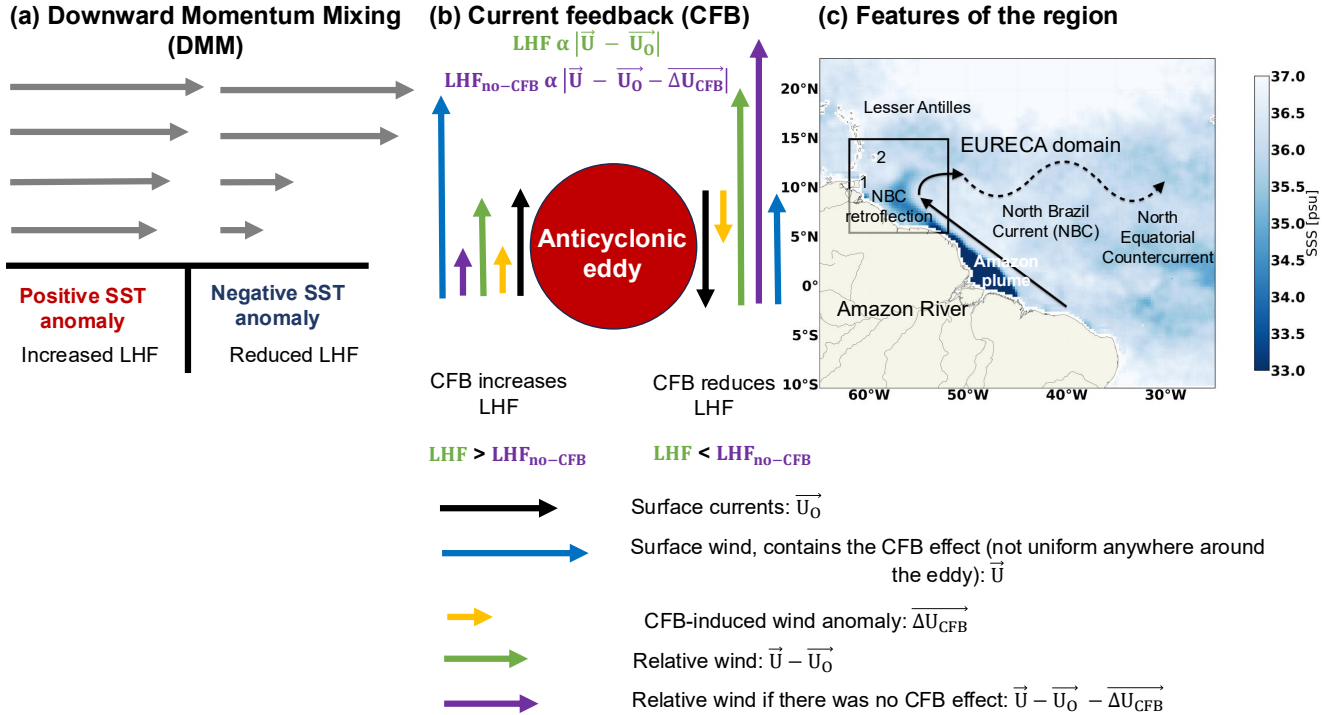
Figure 1. (a) Schematic representation of the Downward Momentum Mixing (DMM) mechanism, adapted from Meroni et al. (2020). (b) Schematic representation of the Current Feedback (CFB) mechanism. Details on how to compute the CFB-induced wind anomaly (ΔU_{CFB}) are provided in subsection 3.1. (c) Major dynamical features of the western equatorial Atlantic (arrows) overlaid on the averaged sea-surface salinity (SSS) field from February 17th–19th, 2020. The SSS field is derived from the SMAP-SSS Level 3, version 4.0, 8-day running-mean gridded product (Boutin et al., 2021). The black box delineates the EURECA region, which corresponds to the simulation domain used in this study. Numbers 1 and 2 mark the locations of Trinidad and Tobago and a region near Barbados, respectively. These geographical references, along with the Lesser Antilles, are used throughout the main text.

in the cold wake of tropical cyclones (Ma et al., 2020) through a cross-track secondary circulation (Pasquero et al., 2021). Finally, Conejero et al. (2025) showed that both PA and DMM are diminished when the model spatial resolution is increased and the full range of mesoscale structures is resolved due to a stronger submesoscale-induced atmospheric frontogenesis. In the Northwest Tropical Atlantic, Fernández et al. (2023) found that DMM dominates over PA using multiple satellite products.

60   In addition to SST effects, surface currents, also influence wind stress and thus surface winds and LHF via a *bottom-up* process known as current feedback (CFB), (Bye, 1985; Chelton et al., 2001; Renault et al., 2016b, a, 2019a). Here, we focus on the CFB-induced surface wind response and its impact on LHF. When surface currents and winds are aligned, an anomalous surface wind develops, reinforcing the prevailing wind field (Renault et al., 2016b). This enhances relative wind speed (the difference between surface wind and surface current velocities) and increases LHF. Conversely, when surface currents oppose

65 surface winds, the CFB-induced wind anomaly weakens surface winds, which could lead to smaller LHF. This process is illustrated in the left and right sides of the eddy in Fig. 1b respectively.

The significance of CFB in eddy dynamics has been highlighted in studies using remote sensing data (Gaube et al., 2015) and high-resolution coupled simulations (Eden and Dietze, 2009; Renault et al., 2016b). Ignoring atmospheric adjustments to CFB might lead to an overestimation of eddy attenuation timescales and an underestimation of eddy amplitude and azimuthal

70 speed. CFB might also shortens eddy lifetimes, as the observed composite life cycle reconstructed from satellite altimetry in (Renault et al., 2016b) and consisting of a rapid early intensification, a prolonged slow CFB-induced decay, and an abrupt collapse at the end seems to suggest. This would imply that CFB systematically acts as an *eddy-killer*, transferring energy from mesoscale eddies to the atmosphere (Anderson et al., 2011; Bye, 1985; Dewar and Flierl, 1987; Oerder et al., 2018; Renault et al., 2016b). Furthermore, an inaccurate representation of CFB in numerical models has implications for biogeochemistry. In

75 oligotrophic regions, mesoscale processes enhance the upward transport of limiting nutrients, supporting biological production (Martin and Richards, 2001; Gaube et al., 2013). In coastal upwelling systems, such as along the Californian coast, eddies modulate biological productivity by subducting nutrients below the euphotic zone and advecting biogeochemical material offshore (Gruber et al., 2011; Nagai et al., 2015; Renault et al., 2016a). Misrepresenting CFB may lead to an overestimation of nutrient quenching and offshore transport, thereby impacting marine ecosystems by altering eddy amplitude, lifetime, and

80 spatial extent.

As stated above, this paper is focused in the Northwest Tropical Atlantic. The ocean circulation in this region, particularly near the Amazon River estuary, is dominated by the North Brazil Current (NBC), as illustrated in Fig. 1c. The NBC is a strong western boundary current originating in the Equatorial and South Atlantic. Around 8°N, it separates from the coast, forming the NBC retroflection, which feeds the North Equatorial Countercurrent. The NBC system is closely linked to two major processes:

85 the Amazon freshwater advection in the open-ocean (Reverdin et al., 2021) and the periodic formation of mesoscale eddies known as NBC rings (Johns et al., 1990; Richardson et al., 1994). These processes are interconnected, as NBC rings facilitate the offshore transport and the lateral spreading of the Amazon river plume induced by mesoscale advection and smaller-scale instabilities (Johns et al., 1990; Fratantoni and Glickson, 2002; Reverdin et al., 2021; Olivier et al., 2022; Coadou-Chaventon et al., 2024). This results in strong spatial heterogeneity in sea surface salinity (SSS, Fig. 1c), which also influences upper

90 ocean temperature by modulating stratification. When low salinity dominates the upper-ocean stratification, the ocean mixed layer (ML), the surface layer in direct contact with the atmosphere, becomes shallower. This can lead to the formation of barrier layers (BLs), which promote temperature inversions (Anderson et al., 1996; de Boyer Montégut et al., 2007; Foltz and McPhaden, 2009; Vialard and Delecluse, 1998; Mignot et al., 2012; Mahadevan et al., 2016; Krishnamohan et al., 2019; Coadou-Chaventon et al., 2024). In the presence of a BL, heat and momentum fluxes remain confined to the shallow ML,

95 which responds more rapidly to atmospheric forcing. Consequently, the ML cools more quickly in winter and warms more rapidly in summer due to the inhibited exchange with deeper ocean layers (Miller, 1976; Sprintall and Tomczak, 1992). This leads to negative (positive) sea surface temperature (SST) anomalies relative to surrounding waters over the Amazon plume and, in turn, reduced (increased) LHF. However, the magnitude of this response remains debated. While observational studies

suggest that BLs have a strong impact on SST (Pailler et al., 1999; Foltz and McPhaden, 2009), numerical models often fail to

100 reproduce this effect (Breugem et al., 2008; Balaguru et al., 2012; Hernandez et al., 2016).

The objective of this study is to investigate how these processes (TFB and CFB) together with the Amazon plume affect LHF variations in the Northwest Tropical Atlantic, complementing previous research based on satellite/reanalysis products (Fernández et al., 2023) and *in-situ* observations (Fernández et al., 2024). To achieve this, we utilize the high-resolution regional coupled simulation described in Conejero et al. (2024). This research is conducted within the framework of the *Elucidating*

105 *the Role of Cloud-Circulation Coupling in Climate – Ocean Atmosphere* (EUREC[4]A-OA) (www.eurec4a.eu) and the *Atlantic Tradewind Ocean-Atmosphere Mesoscale Interaction Campaign* (ATOMIC) (https://psl.noaa.gov/atomic/) field experiments. The paper is structured as follows: Section 2 describes the simulation configuration. Section 3 presents the methods used to analyze model data. The main results are discussed in Section 4, followed by conclusions and future perspectives in Section 5.

2 Data

110 This study utilizes the EURECA ocean-atmosphere coupled simulation (Conejero et al., 2024). The ocean component is based on the Coastal and Regional Ocean COmmunity (CROCO) model (Shchepetkin and McWilliams, 2005; Debreu et al., 2012), while the atmospheric component employs the Weather Research and Forecasting (WRF) model (Skamarock et al., 2008). The two models are coupled via OASIS (Craig et al., 2017), which performs the grid interpolation and temporal averaging for property exchanges between the two model components every hour. Specifically, the ocean model provides SST and surface

115 currents to the atmosphere, while WRF returns surface heat, momentum, and water fluxes to CROCO. Further details on the EURECA simulation configuration are available in Conejero et al. (2024).

The EURECA simulation spans from January 2019 to June 2020, though this study focuses on the January–February 2020 (JF) period. The CROCO domain extends from $5.5°$N to $15.5°$N and $62°$W to $52°$W, with a horizontal resolution of 1 km. Initial and lateral open boundary conditions are provided by the "Antilles" simulation, which employs the same coupled configuration

120 but at a coarser resolution over a larger domain, including parts of the Caribbean Sea (Conejero et al., 2025).

The WRF domain in EURECA is slightly larger than the ocean domain to mitigate sponge effects. The atmospheric model runs at a horizontal resolution of approximately 2 km, with outputs available on 40 η vertical levels. To analyze the first 2000 m of the atmosphere, these levels are linearly interpolated to uniform 100 m vertical spacing. Initial and boundary conditions, provided by the "Antilles" simulation, are updated every 3 hours. Bulk formulations (Fairall et al., 2003) are used to estimate

125 freshwater, turbulent, and momentum fluxes, which are then fed into the ocean model. The CFB effect is implemented in both the surface and planetary boundary layer schemes, following Renault et al. (2019a). WRF variables at multiple vertical levels are stored every 3 hours, while surface variables are recorded hourly.

3   Methodology

Following Fernández et al. (2024), we remove the diurnal cycle from all variables before analyzing LHF sensitivity to the
130   surface ocean. This is achieved by computing daily means from the WRF/CROCO outputs, and all subsequent calculations are
performed on these averaged variables. It is important to note that this procedure filters out part of the ocean submesoscale
variability. Consequently, this paper deals exclusively with the ocean mesoscale. We briefly return to this point in Section 5.

All analyses are performed in four regions. First, we consider the full simulation domain, referred to as the EURECA domain
($5.5°-15°$N, $62°-52°$W). Additionally, we examine three distinct sub-regions: Amazon ($7°-9°$N, $56°-53°$W), Downstream
135   ($9°-11°$N, $59°-56°$W) and Tradewind ($12°-14°$N, $58°-52.5°$W). Fig. 2 displays three black boxes delineating the sub-
regions. The three subdomains are characterized by different ocean dynamics and air-sea interactions. The Tradewind sub-
region, representative of the open ocean, is relatively quiescent, whereas the Downstream sub-region, closer to the coast,
exhibits enhanced *fine-scale* ocean activity, and the Amazon sub-region is influenced by the Amazon plume. These regional
differences have been highlighted in previous studies based on remote sensing and reanalysis data (Fernández et al., 2023) as
140   well as *in-situ* observations (Fernández et al., 2024). To ensure consistency with these studies, all analyses are restricted to the
January–February (JF) 2020 period.

3.1   Coupling Coefficients

Following Renault et al. (2016b, 2019b) and Conejero et al. (2024), we estimate several air-sea coupling coefficients as the
statistically significant slope (determined via a two-sided *t*-test) of the linear regression between the binned distributions of
145   mesoscale anomalies from two variables. For all coefficient calculations, we exclude mesoscale anomalies located on the
continental shelf (regions where the seafloor is shallower than 100 m) and the Lesser Antilles (west of $60.25°$W), as these
areas can be affected by orography, land-sea interactions, and coastline effects (Desbiolles et al., 2014).

To compute mesoscale anomalies we use a combination of time and spatial filters. In order to remove weather-induced
synoptic variability from the atmospheric variables (winds, specific humidity, and air temperature), we first apply a 29-day
150   running mean as in Chelton et al. (2007); Renault et al. (2019b); Conejero et al. (2024). To isolate the mesoscale band, we
apply a band-pass isotropic Gaussian filter with a 50–250 km cutoff length (Renault et al., 2019b), to the 29-day running mean
dataset and keep the scales between 50 and 250 km. After performing the filtering for the whole EURECA domain, we select
the anomalies in Amazon, Downstream and Tradewind to operate on them separately.

To characterize the effect of surface currents on near-surface winds (CFB) we compute s_w, the coupling coefficient between
155   surface current vorticity and surface wind curl anomalies (Renault et al., 2016b, 2019b). Note that, since mesoscale currents
are nearly in geostrophic balance (and therefore non-divergent), s_w effectively isolates the CFB from the TFB at the mesoscale
(Renault et al., 2019b). Using s_w, the CFB-induced wind anomaly ($\overrightarrow{\Delta U_{CFB}}$) reads:

$$\overrightarrow{\Delta U_{CFB}} = s_w \overrightarrow{U_o}, \tag{1}$$

where $\overrightarrow{U_o}$ stands for surface currents. Recall that $\overrightarrow{\Delta U_{CFB}}$ is represented in orange arrows in Fig. 1b.

Coupling Coefficient	Description
s_w	surface current vorticity and surface wind curl
s_u	SST and surface wind magnitude
s_q	SST and surface specific humidity
s_t	SST and surface temperature

Table 1. Overview of the coupling coefficients.

Finally, we also calculate the coupling coefficients of near-surface wind speed (s_u), near-surface specific humidity (s_q) and near-surface atmospheric temperature (s_t) mesoscale anomalies with respect to SST mesoscale anomalies. Table 1 provides a summary of the coupling coefficients described above.

3.2 LHF Sensitivity to SST and Surface Currents

To evaluate how LHF responds to SST and surface currents, we compute multiple LHF datasets using the COARE3.5 algorithm (Edson et al., 2013). First, we calculate LHF_U, which represents the LHF dataset obtained using the atmospheric variables of the first WRF vertical level (surface winds, air temperature and specific humidity) together with SST. Note that we do not consider relative winds (i.e. the difference between surface winds and surface currents) to compute LHF_U. Additionally, we compute LHF_{LR}, which corresponds to LHF computed with the *smoothed* same variables as LHF_U, obtained by applying a Gaussian low-pass filter (cutoff length of 250 km) to the original WRF variables and SST. Again, we do not consider relative winds in the calculation of LHF_{LR} either.

We then apply the LHF downscaling algorithm developed by Fernández et al. (2023). Given a *smoothed* variable (Ψ_{LR}), we reconstruct a new dataset incorporating the finer-scale SST features (Ψ_{HR}) as:

$$\Psi_{HR} = \Psi_{LR} + s_\psi \Delta SST. \tag{2}$$

Here, ΔSST represents the SST correction, which accounts for deviations of the high-resolution SST field from the coarse *smoothed* SSTs. To ensure that the domain-averaged SST correction is zero and that the area-weighted means of the variables remain conserved, ΔSST is computed as:

$$\Delta SST = \left(SST - \overline{SST} \right) - \left(SST_{LR} - \overline{SST_{LR}} \right). \tag{3}$$

$\overline{\text{Overbars}}$ denote the spatial average over the region of study. Thus, to compute LHF_{HR}, we statistically downscale each of the variables driving LHF (surface wind, specific humidity air temperature and SST) using its corresponding coupling coefficient, as detailed above, and we then apply COARE3.5 with the downscaled variables. Note that we do not use relative winds for LHF_{HR} either.

To isolate the thermodynamic contribution (i.e. LHF variations solely due to SST changes via modifications of the saturation specific humidity) to LHF sensitivity, we compute an additional LHF dataset, denoted as $\text{LHF}_{\text{therm}}$. In this dataset, air temperature and SST are downscaled, while wind speed remains with its *smoothed* value. The specific humidity required to obtain $\text{LHF}_{\text{therm}}$ is derived from the *smoothed* relative humidity and the specific humidity of saturation computed with SST_{HR} via the Clausius-Clapeyron equation. This ensures that the specific humidity variations for this LHF subset are only due to SST mesoscale changes themselves without the effects of the atmospheric-induced modifications of mesoscale SST structures (i.e. entrainment of drier air from the free troposphere associated with DMM).

Moreover, we compute $\text{LHF}_{\text{therm}-\text{U}}$ to further distinguish, within the dynamic contribution, the effects of wind speed and specific humidity. Recall that the dynamic contribution represents LHF changes associated with the mesoscale SST-induced modifications of the near-surface atmosphere (winds and specific humidity). Thus, in $\text{LHF}_{\text{therm}-\text{U}}$, air temperature, and surface winds are downscaled, while specific humidity is obtained as in $\text{LHF}_{\text{therm}}$. This means that the only change between LHF_{HR} and $\text{LHF}_{\text{therm}-\text{U}}$ is that specific humidity in the latter is scaled maintaining relative humidity at its *smoothed* value whereas in the former, specific humidity is downscaled with Eq. 2. Thus, $\text{LHF}_{\text{therm}-\text{U}}$ accounts for both the thermodynamic contribution to LHF sensitivity to SST and the effect of SST-induced mesoscale surface wind changes.

Finally, to assess the contributions of surface currents in LHF variations, we consider two additional LHF datasets. LHF_{orig} is computed using the original WRF variables in COARE3.5, but replacing the first vertical model-level wind speed with relative winds. Thus, the difference $\text{LHF}_{\text{orig}} - \text{LHF}_{\text{U}}$ represents the variations in LHF associated with the consideration of relative winds instead of just surface winds when computing LHF. Meanwhile, $\text{LHF}_{\text{no}-\text{CFB}}$ stands for LHF computed with relative winds, but with the CFB-induced wind anomaly ($\overrightarrow{\Delta\text{U}_{\text{CFB}}}$, Eq. 1, represented in orange arrows in Fig. 1b) removed component-wise. Hence, $\text{LHF}_{\text{orig}} - \text{LHF}_{\text{no}-\text{CFB}}$ contains the CFB effect on LHF.

3.3 Mixed Layer Heat Budget

To provide a broader insight on the linkages between the mesoscale SST anomalies leading to LHF variations and the Amazon River plume, we present a mixed layer heat budget analysis in the Amazon sub-region. The temperature equation, vertically integrated down to the mixed layer depth reads (Vialard and Delecluse, 1998):

$$\underbrace{\langle\partial_t\text{T}\rangle_\text{H}}_{\text{Total tendency}} = \underbrace{\langle-\text{u}\partial_x\text{T} - \text{v}\partial_y\text{T}\rangle_\text{H}}_{\text{Horizontal advection}} - \underbrace{\langle\text{w}\partial_z\text{T}\rangle_\text{H}}_{\text{Vertical advection}} + \overbrace{\underbrace{\frac{\text{Q}_\text{s}\left(1 - \text{F}_\text{H}\right) + \text{Q}_\text{ns}}{\rho_0\text{C}_\text{p}\text{H}}}_{\text{Atmospheric forcing}}}^{\text{Forcing }\mathcal{F}} +$$
$$+ \overbrace{\underbrace{\frac{\partial_t\text{H}}{\text{H}}\left(\text{T}_\text{H} - \langle\text{T}\rangle_\text{H}\right)}_{\text{Entrainment}}}^{\text{Mixing }\mathcal{D}} + \text{Residual} \quad\quad (4)$$

where angle brackets ($\langle\rangle$) indicate integration down to the base of the mixed layer. To facilitate interpretation, the mixed layer depth (MLD) is denoted as H in Eq. 4. In this equation, T represents the ocean temperature, u, v, and w denote the zonal,

210   meridional, and vertical currents, respectively, and T_H is the temperature at the base of the mixed layer.

The MLD is computed using a density threshold criterion of $\Delta\sigma = 0.01$ kg m^{-3}, following Gévaudan et al. (2021). This criterion yields MLD values consistent with *in-situ* observations reported by Fernández et al. (2024). In Eq. 4, Q_s represents the solar component of the total heat flux, primarily shortwave radiation (SW). F_H denotes the fraction of solar radiation reaching the ML base. The term Q_{ns} represents the non-solar component of the total heat flux, which can be expressed as:

215 $$Q_{ns} = \underbrace{\underbrace{DLW}_{\text{Downward longwave radiation}} - \underbrace{ULW}_{\text{Upward longwave radiation}}}_{\text{Radiative heat fluxes}} - \underbrace{\underbrace{LHF}_{\text{Latent heat flux}} - \underbrace{SHF}_{\text{Sensible heat flux}}}_{\text{Turbulent heat fluxes}}. \tag{5}$$

Here, DLW, LHF, and SHF are obtained from WRF, while ULW is computed using Stefan-Boltzmann's law. Note that the flux sign convention differs when computing the MLD heat budget compared to the atmospheric convention: fluxes directed from the ocean to the atmosphere are considered negative, as they contribute to ML cooling. Finally, the EURECA simulation employs the COARE3.0 bulk formulae (Fairall et al., 2003) to compute turbulent heat fluxes (THFs). For consistency, model-

220   derived THFs are used when calculating the ML heat budget. However, we used COARE3.5 (Edson et al., 2013) to assess LHF sensitivity to SST and surface currents. This does not lead to any inconsistency in the results, since we always compare between LHFs computed with the same algorithm. In addition, we verified that the differences between both algorithms are small compared to the LHF difference values obtained in this article.

Finally, the Residual term in Eq. 4 accounts for horizontal and vertical diffusion, as well as numerical errors associated

225   with the computation of the other terms. The reader is referred to Section A of the Appendix for further details on the most appropriate way to compute the Residual to minimize numerical errors. Additionally, we explore various criteria to determine whether vertical or horizontal diffusion dominates the Residual in Section B of the Appendix.

Another important quantity used to analyze the effects of water temperature in vertical stratification is the base of the isothermal layer (THERM). Like in Gévaudan et al. (2021), we estimate it as the depth at which the water temperature is

230   0.2°C lower than the 10 m depth level temperature. Therefore, the barrier layer thickness (BLT) results from the difference between THERM and MLD. Finally, to quantify the relative importance of salinity in ocean stratification, we use the Ocean Stratification Strength (OSS) indicator (Gévaudan et al., 2021; Maes and O'Kane, 2014):

$$OSS = \frac{N_S^2}{N^2}. \tag{6}$$

Here, N^2 represents the Brunt-Väisälä frequency, while N_S^2 denotes the Brunt-Väisälä frequency computed using a constant

235   representative temperature, allowing only for salinity variations. OSS values greater than 50% indicate that salinity dominates over temperature in controlling ocean vertical stratification.

4 Results

4.1 Air-Sea Interface

Fig. 2 presents the JF 2020 mean state of different air-sea interface variables in the Northwest Tropical Atlantic. The shading
240   in Fig. 2a represents SST, highlighting a warm water stripe ($> 27.3°$C) along the South American coast, extending from the
southernmost coastal point in the domain to Trinidad and Tobago. To its east, a parallel cold SST band ($< 25.5°$C) borders
Trinidad and Tobago and extends northward towards the Lesser Antilles. Further offshore, SST values remain relatively homo-
geneous ($27°$C), though localized anomalies are observed, such as the warmer region to the east of the Amazon subdomain,
associated with the northward advection of warm Amazon plume waters (not shown). Contours in Fig. 2a show first vertical
245   level specific humidity, which is highest near the South American coast and decreases towards the northeast.

Fig. 2b displays near-surface wind speed (contours), which varies between 7.5 and 8.2 m s^{-1}. The LHF spatial pattern
(shading) closely follows the SST distribution in Fig. 2a, with the highest LHF values (> 180 W m^{-2}) occurring over the
warm coastal stripe and in the open ocean, and the lowest values (< 100 W m^{-2}) located over the cold SST band extending
across the continental shelf. Other patches of relatively low LHF are observed offshore over cooler SSTs wuch as the ones west
250   to Barbados and the Amazon sub-region.

To further characterize the atmospheric JF 2020 spatial pattern, Fig. 2c presents the MABLH (shading) and surface winds
(arrows). Consistent with the DMM mechanism, the shallowest MABL depths (< 500 m) align with the cold SST stripe,
whereas deeper MABL values occur over the open ocean, where SSTs and wind speeds are higher. The dominant wind direction
shifts from easterly in the open ocean to northeasterly (trades) closer to the coast. Fig. 2d displays surface currents (arrows) and
255   SSS (shading). In the southeastern domain, strong northwesterly currents (NBC) advect a low-salinity patch (SSS < 35 psu)
associated with the Amazon plume, whose shape and extent are modulated by local eddy-driven circulation. Near Trinidad and
Tobago, a second region of enhanced surface currents exhibits a clockwise rotation, at $10°$N, $58°$W. This eddy, which remains
nearly stationary during JF 2020, lacks strong SSS and SST surface signatures. Such signatures are observed when studying
its vertical structure (not shown).

4.2   Coupling Coefficients

To assess the relation between SST/surface current anomalies and the near surface atmosphere at the mesoscale, we compute
the coupling coefficients as defined in Subsection 3.1. Note that these coupling coefficients will be needed to statistically
downscale each of the LHF controlling variables (Eq. 2) in following sections. Since the ocean dynamics is different between
sub-regions, we compute the coupling coefficients separately in EURECA, Amazon, Downstream and Tradewind. Fig. 3,
265   illustrates the value of the coupling coefficients and the binned linear regressions are displayed in Section C of the Appendix.

The first four salmon markers in Fig. 3 present the spatial distribution of the slope of the linear regression between the
mesoscale surface current vorticity and surface wind curl anomalies. Recall that this linear regression results in the cou-
pling coefficient named s_w, used to assess the CFB. The intensity of s_w can be interpreted as the efficiency of the partial
re-energization of the ocean through the wind response to CFB (Renault et al., 2016b, 2019b). Mesoscale s_w values range
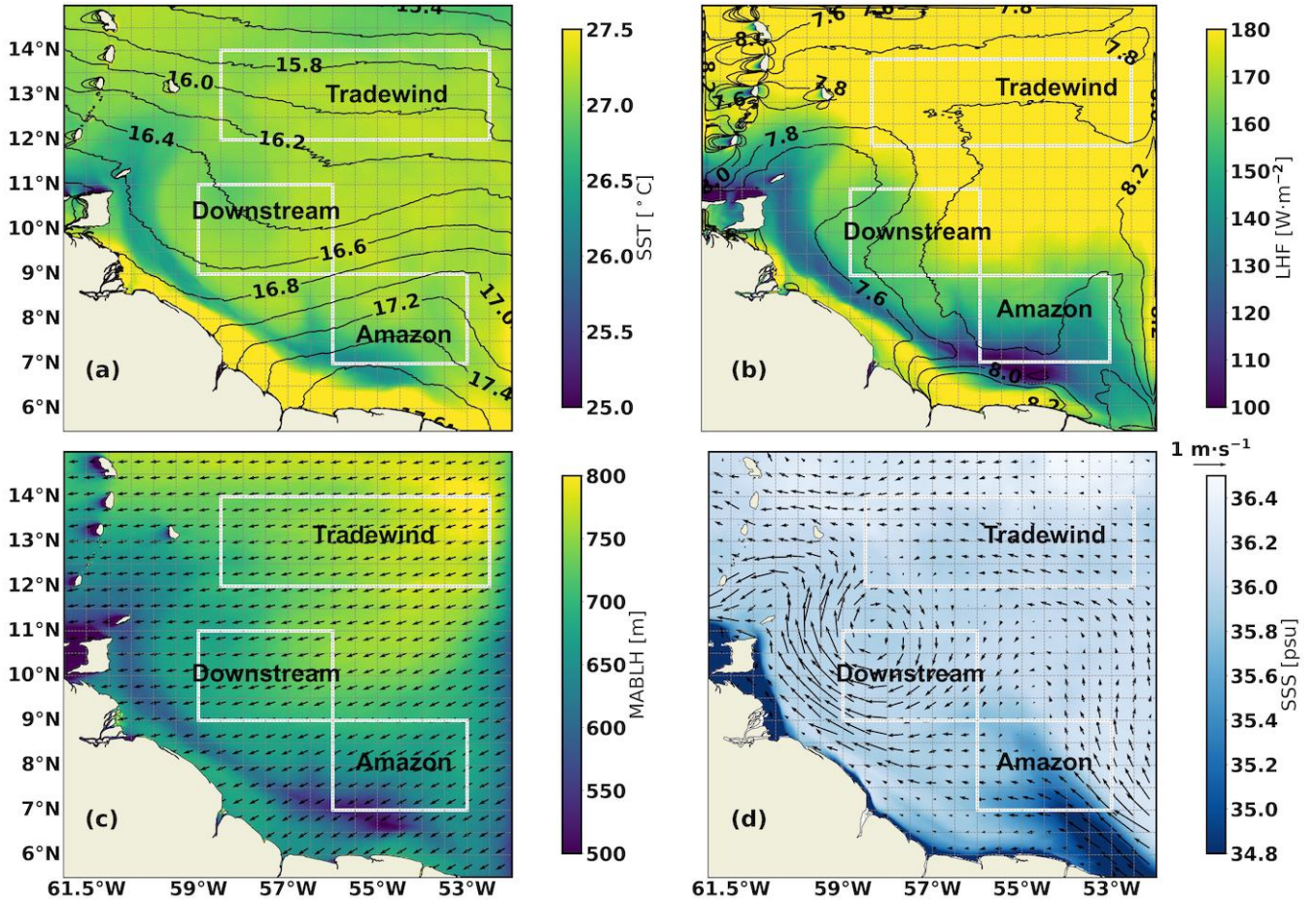
Figure 2. JF 2020 mean of (a) SST (in °C, shaded) and near-surface specific humidity (in g kg^{-1}, contours), (b) LHF (in W m^{-2}, shaded) and near-surface wind speed (in m s^{-1}, contours), (c) MABLH (in m, shaded) and surface winds (arrows), and (d) SSS (in psu, shaded) and surface currents (in m s^{-1}, arrows). In all panels, from north to south, the three white boxes delineate the Tradewind, Downstream, and Amazon sub-regions.

from 0.22 to 0.28, with weaker coupling in the Amazon and Tradewind subdomains (0.22 and 0.24 respectively). The strongest mesoscale coupling is found in EURECA and in the Downstream subdomain, where s_w reaches 0.28 and 0.26 respectively.

In other words, these s_w values indicate that a mesoscale eddy with a velocity of 1 m s^{-1} induces, on average, a wind speed anomaly of 0.28 m s^{-1} in the EURECA domain, which in turn influences LHF estimations through changes in surface winds as shown in Fig. 1b. They also show the spatial variability in the strength of the coupling. The interactions are stronger within the in Downstream than in Tradewind (open ocean).

s_u is displayed in the second four cyan markers of Fig. 3. It is positive in the four domains: warm (cold) SST anomalies increase (decrease) surface winds, which is consistent with the DMM mechanism. s_u is weaker in Tradewind (open ocean,
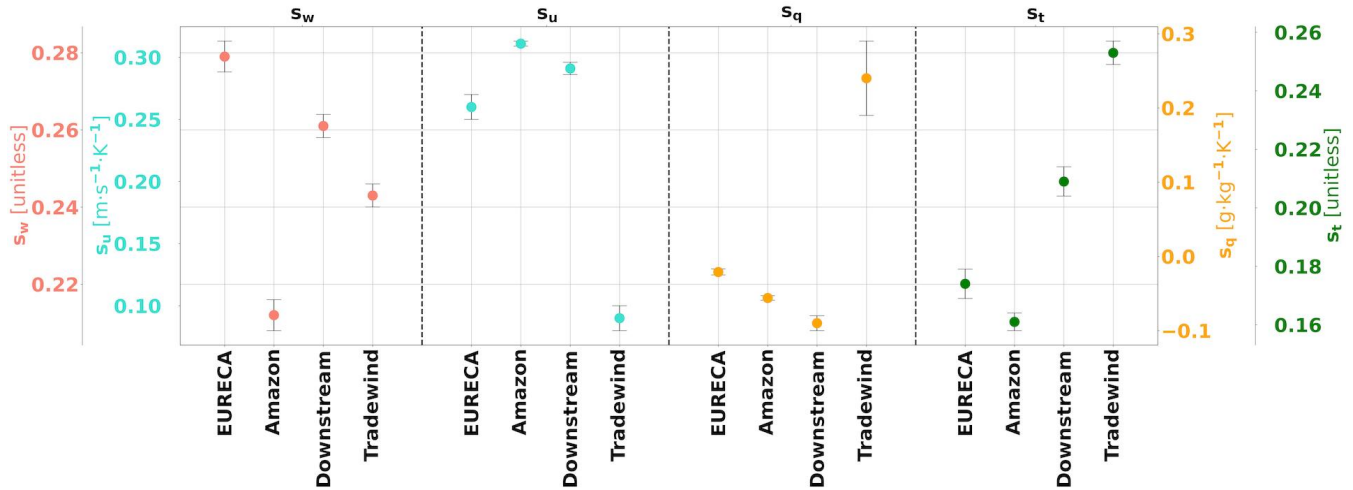
11

Figure 3. Mesoscale coupling coefficients s_w (salmon), s_u (cyan), s_q (orange) and s_t (green). In each dot quartet, from left to right, the markers represent the corresponding coupling coefficient in the EURECA, Amazon, Downstream and Tradewind domains respectively. The error bars depict the standard error of the slope. All the coefficients displayed here are statistically significant at the 95% level after a two-sided *t*-test.

0.11 m s^{-1} K^{-1}) than in Amazon and Downstream (warm eddy corridor, 0.29 and 0.31 m s^{-1} K^{-1} respectively). This feature has been previously found in Fernández et al. (2023) using satellite observations. The entire EURECA region produces a s_u of

280   0.26 m s^{-1} K^{-1} which is in agreement with the January-February-March s_u of Conejero et al. (2024) using the same simulation and hourly data (see their Fig. 9h).

Another key variable driving LHF is near-surface specific humidity (q). As with wind speed, we use the specific humidity from the first vertical level in the WRF simulation at about 10 m. The four orange markers in Fig. 3 show the associated coupling coefficient s_q. It exhibits weak negative values over the Amazon (-0.05 g kg^{-1} K^{-1}), Downstream (-0.09 g kg^{-1} K^{-1}) and

285   EURECA (-0.03 g kg^{-1} K^{-1}, in agreement with Fernández et al. (2023)), while a stronger positive value appears associated with the Tradewind subdomain (0.24 g kg^{-1} K^{-1}). The underlying physical explanation is as follows: at scales larger than the mesoscale, evaporation is sufficient for specific humidity to adjust to SST according to the Clausius-Clapeyron equation. This adjustment rate was estimated to be 1.3 g kg^{-1} K^{-1} through linearization of the Clausius-Clapeyron equation in Fernández et al. (2023). However, at the mesoscale this equilibrium does not hold, as q does not have sufficient time to adjust to SST

290   variations, resulting in a weak correlation between the two variables. Note that in Amazon and Downstream, the mesoscale s_q is negative meaning that specific humidity decreases with increasing SST. This behavior may reflect the entrainment of colder and drier air from the free troposphere due to the DMM mechanism. We will come back to this point later.

Finally, the last four green markers in Fig. 3 represent s_t in the different domains. As expected, they all are positive: higher SST implies higher surface air temperature. In addition, s_t is strongest in Tradewind ($\sim$0.25) where the SST-associated wind

295 speed and specific humidity variations are weaker. This might result from a decreased advection of other air masses with other temperatures which could locally modify temperature values close to the surface.

4.3 LHF Sensitivity to SST and Currents

To evaluate the representation of LHF sensitivity to SST in the EURECA simulation, we perform a linear regression between LHF variations and the SST correction (ΔSST, see Eq. 3) for the different LHF subsets detailed in Subsection 3.2. The results

300 are presented in Fig. 4 for the EURECA domain (first row), the Amazon sub-region (second row), the Downstream sub-region (third row), and the Tradewind sub-region (fourth row).

The estimated LHF change per °C associated with the presence of the mesoscale ocean is shown in orange in Figs. 4a, c, e, and g, representing the difference between LHF_{HR} and LHF_{LR}. Recall that LHF_{HR} is computed using the statistically downscaled WRF variables (Eq. 2) in COARE3.5, while LHF_{LR} corresponds to LHF derived from the *smoothed* variables,

305 obtained by subtracting low-pass filtered values (Gaussian filter with a 250 km cutoff length) from the raw data.

The mean LHF sensitivity to mesoscale SST in the EURECA region is 47.7 W m^{-2} K^{-1} and the Amazon and Downstream sub-regions show similar values (46.7 W m^{-2} K^{-1} and 46.9 W m^{-2} K^{-1} respectively). On the contrary, the sensitivity is lower in the Tradewind subdomain (35 W m^{-2} K^{-1}). Given the mean LHF values of 150 W m^{-2} in EURECA, 130 W m^{-2} in Amazon, 170 W m^{-2} in Downstream, and 140 W m^{-2} in Tradewind, the slopes of the linear regressions correspond to

310 31.8 % K^{-1} (47.7/150), 35.9 % K^{-1} (46.7/130), 27.5 % K^{-1} (46.9/170), and 25 % K^{-1} (35/140), respectively. These values align with the theoretical estimate of approximately 33 % K^{-1} of Fernández et al. (2023). In addition, they are consistent with satellite (33.8 % K^{-1}) and reanalysis (26.6 % K^{-1}) estimates obtained in Fernández et al. (2023). The observed regional differences were also reported in that study, with stronger LHF variations near the South American coast (Amazon and Downstream) compared to the open ocean (Tradewind). Finally, Conejero et al. (2024), using the same simulation, computed the

315 sensitivity of THF mesoscale anomalies with respect to SST mesoscale anomalies. They obtained a value of 53 W m^{-2} K^{-1} in January-February-March for the whole EURECA region, slightly larger than our 47.7 W m^{-2} K^{-1} (see their Fig. 10). This is partly because of the effect of sensible heat flux (present in the THF) which adds to the LHF sensitivity to SST and partly due to the fact that we consider JF.

We compare the LHF sensitivity results with *in-situ* observations as well. In Fernández et al. (2024), the LHF changes

320 were assessed across mesoscale SST anomalies of 2°C and −0.4°C, in the Amazon and Downstream sub-regions, respectively. The first SST anomaly induced a LHF difference of approximately 160 W m^{-2} between itself and its environment (∼80 W m^{-2} K^{-1}). The second SST anomaly, resulted in a LHF difference of 95 W m^{-2} (∼38 W m^{-2} K^{-1}). Therefore, the latter agrees better with the model estimate for the Downstream subdomain, while the former is significantly larger, likely due to its proximity to the coast. Indeed, the strongest SST gradients in the model also appear over the continental shelf (Fig. 2a)

325 and are not included in this analysis. We should also keep in mind that LHF sensitivity to SST across fronts in *in-situ* observations is subject to several uncertainty sources which could modify its value and make the direct comparison with model estimates less straightforward. The relative orientation between the sampling device's trajectory and the SST front or even just defining the front's location are amont these uncertainty sources.
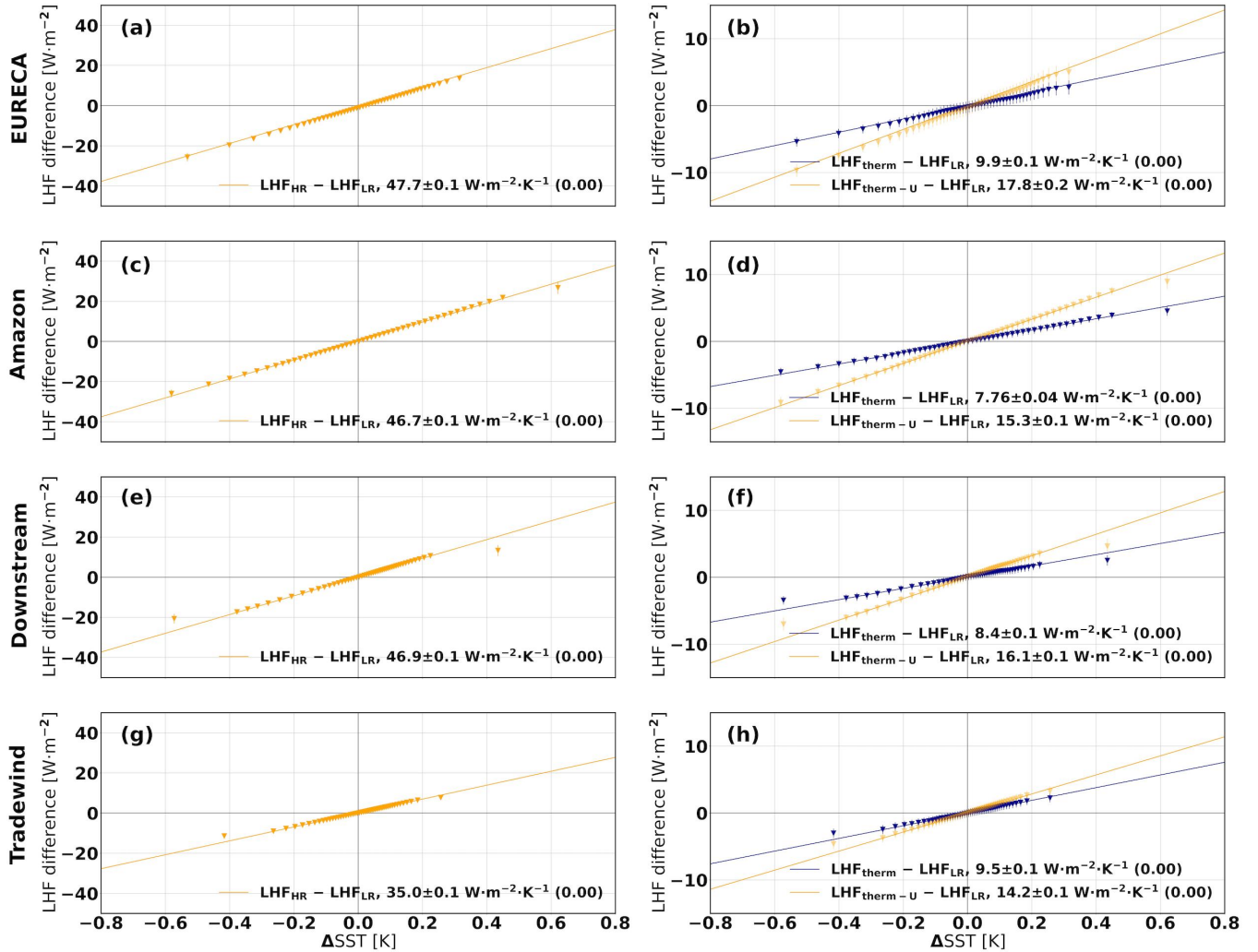
Figure 4. LHF sensitivity to ΔSST (see Eq. 3) across different regions. Each row corresponds to a specific domain: the EURECA region (first row), the Amazon sub-region (second row), the Downstream sub-region (third row), and the Tradewind sub-region (fourth row). Panels (a), (c), (e), and (g) display the difference between LHF_{HR} and LHF_{LR} as a function of ΔSST. Panels (b), (d), (f), and (h) show the differences between LHF_{therm} and LHF_{LR}, and between $LHF_{therm-U}$ and LHF_{LR}, as a function of ΔSST (blue and orange, respectively). The methodology used to compute these LHF datasets is detailed in the main text. The SST anomaly values are binned into 2% percentile intervals, ensuring each contains more than 15 000 values. Vertical error bars indicate the standard deviation from the mean in each interval, while straight lines represent the least-squares regression fits. The regression slope $\pm$ standard error (p-value) is reported at the bottom of each panel.

To quantify the thermodynamic contribution to LHF sensitivity (i.e. the component linked only to SST changes, denoted as
330    $\text{LHF}_{\text{therm}}$), we compute its linear regression shown in dark blue in Figs. 4b, d, f, and h. In the EURECA domain, this contribution accounts for a LHF change of 6.6% K^{-1} (9.9/150). In the other sub-regions, it represents 6 % K^{-1} (Amazon, 7.76/130), 4.9 % K^{-1} (Downstream, 8.4/170) and 6.7 % K^{-1} (Tradewind, 9.5/140). The increasing importance of the thermodynamic contribution towards the open ocean is consistent with the particular air-sea coupling in these regions (lower s_u and s_t and larger s_q, see Fig. 3). Overall, these LHF sensitivity values show that in the presence of mesoscale anomalies, LHF variation at
335   the mesoscale are mainly associated with the dynamic contribution (i.e LHF variations linked to the SST-induced modification of the near-surface atmospheric variables) whereas the thermodynamic contribution remains a second-order contributor, in agreement with previous observation and reanalysis-based studies (Fernández et al., 2023).

For completeness, we also compute $\text{LHF}_{\text{therm}-U} - \text{LHF}_{\text{LR}}$ as a function of ΔSST, shown in orange in Figs. 4b, d, f, and h. This allows us to separate the surface wind contribution from the specific humidity's within the dynamic component of
340   LHF sensitivity. In EURECA, Amazon and Downstream the effect of surface wind variations adds around 8 W m^{-2} K^{-1} to the thermodynamic contribution. Regarding Tradewind, the wind speed contribution is more modest, representing only an additional 4.7 W m^{-2} K^{-1}. Therefore, within the dynamic contribution, the majority of the LHF change is linked to the weak mesoscale SST-specific humdity coupling. The air temperature effect is even smaller than the wind speed and it is not shown here for the sake of simplicity.

345   To quantify the impact of using relative winds (i.e., surface winds minus currents) in LHF computations, we perform a linear regression between $\text{LHF}_{\text{orig}} - \text{LHF}_U$ and the difference between the norms of relative winds and surface winds. Here, LHF_U represents the dataset computed using only the closest-to-the-surface winds (without currents) and LHF_{orig} stands for the LHF computed using relative winds. The regressions are shown in dark blue in Fig. 5 for the EURECA (a), Amazon (b), Downstream (c), and Tradewind (d) regions.

350   Across the EURECA domain, surface wind speed generally exceeds relative wind speed. Winds predominantly blow towards the southwest ($-110°$ from north), while surface currents are oriented northwestward ($-70°$ from north). As a result, considering only surface winds increases LHF by up to 10 W m^{-2}, a trend observed across all sub-regions. The sign and magnitude of $\text{LHF}_{\text{orig}} - \text{LHF}_U$ depend on the relative orientation of winds and currents. In the Downstream sub-region (Fig. 5c), the southern edge of an anticyclonic eddy (Fig. 2d) aligns surface currents with surface winds ($-120°$ from the north), leading to
355    $|\vec{U}| > |\vec{U}\text{-}\vec{U_o}|$ and thus reducing LHF when relative winds are used. On the contrary, Amazon and Tradewind (Fig. 5b and d) exhibit both positive and negative LHF differences, consistent with its broader wind and surface current distributions (Figs. 2c and d). These LHF variations align well with observations. Using the same representative LHF values for each sub-region, we find that the regression slopes correspond to 10.9, 11.3, 9.4, and 13 % K^{-1} in the EURECA, Amazon, Downstream, and Tradewind regions, respectively. *In-situ* observations report a sensitivity range of 5 % K^{-1} to 15 % K^{-1} (Fernández et al.,
360   2024).

Finally, to isolate the CFB contribution to LHF variations, we perform a linear regression between $\text{LHF}_{\text{orig}} - \text{LHF}_{\text{no}-\text{CFB}}$ and the difference between relative wind norms with and without current feedback. The results, shown in orange in Fig. 5, exhibit a similar sensitivity than the regression concerning $\text{LHF}_{\text{orig}} - \text{LHF}_U$. Whereas $|\vec{U}\text{-}\vec{U_o}|$ is typically smaller than $|\vec{U}|$,
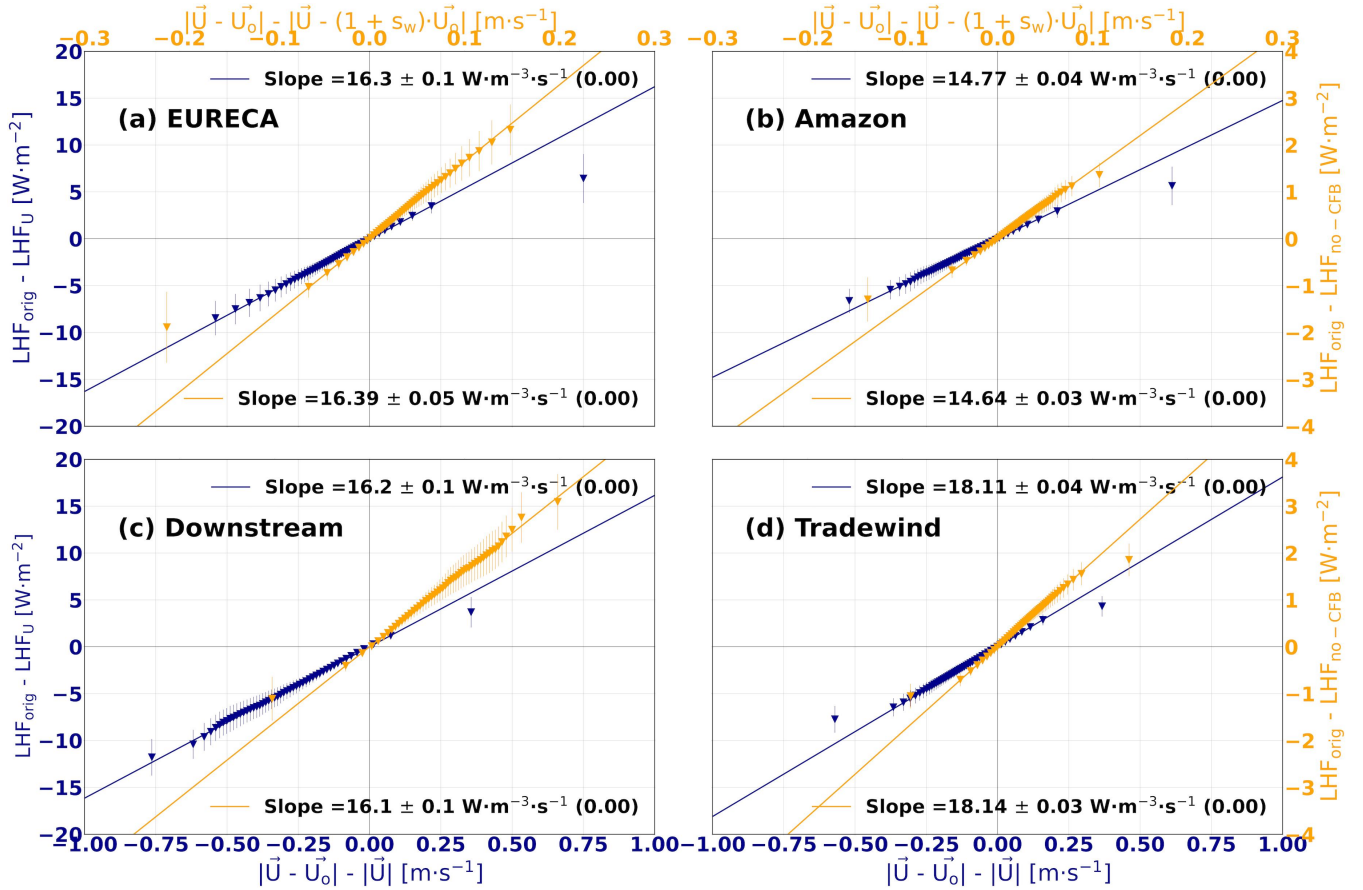
Figure 5. LHF sensitivity to surface currents for (a) EURECA, (b) Amazon, (c) Downstream, and (d) Tradewind. In all panels, blue markers represent the difference between LHF_U and LHF_{orig} as a function of the difference between the norm of the first vertical level wind velocity and the relative wind velocity field. Orange markers indicate the difference between LHF_{orig} and LHF_{no-CFB} as a function of the difference between the norms of relative winds, with and without the CFB effect. The methodology used to derive these LHF datasets is detailed in the main text. The x-axis variable is divided into intervals containing an equal number of values, using a 2% percentile separation, ensuring more than 15 000 values per interval. Vertical error bars indicate the standard deviation relative to the mean for each interval, while straight lines denote the least-squares regression fits. The regression slope ± standard error (p-value) is displayed in each panel's legend.

the relative velocity in presence of CFB is typically larger than the relative velocity without CFB. In addition, the CFB effect is
365   one order-of-magnitude smaller (within ± 3 W m^{-2}), consistent with *in-situ* results from Fernández et al. (2024). According to CFB, surface currents generate wind anomalies in their own direction. Thus, in the Downstream region, where surface currents mostly align with wind direction, CFB enhances relative winds and LHF. In regions without a dominant current direction, LHF variations can be either positive or negative.

4.4 Vertical Ocean and Atmosphere Structure in Amazon

370 To fully explain the modeled LHF variations, we examine the atmospheric response and oceanic configuration associated with mesoscale SST anomalies. Here, we focus on the Amazon sub-region, since we aim to link the mesoscale SST anomalies to the presence of the Amazon plume and its heat budget. Results for the Downstream and Tradewind sub-regions and EURECA yield similar conclusions in terms of physical mechanisms at play and for brevity we do not include them in this study. The analysis follows what is presented in Borgnino et al. (2025) for an atmosphere-only model forced with realistic SSTs.

375 Fig. 6 presents the binned distribution of the marine atmospheric boundary layer (MABL) vertical structure, as well as the dependence of SST, SSS, and mixed layer depth (MLD) on the SST mesoscale anomaly. Over cold SST anomalies, the MABL exhibits increased stability, characterized by positive values of the Brunt-Väisälä frequency anomalies (N^2), particularly above the MABL height (black line in Fig. 6a). Conversely, over warm SST anomalies, the atmosphere becomes more unstable, with negative values of N^2.

380 Changes in atmospheric vertical stratification also influence wind speed variations (Fig. 6b). Two distinct anomaly dipoles are observed at the warmest and coldest ends of the histogram. Over the highest SST anomalies, wind speed increases slightly near the surface (around 0.05 m s^{-1}), while negative wind speed anomalies dominate above. This behavior aligns with the downward momentum mixing (DMM) mechanism: downward fluxes of momentum from the free troposphere reduce wind speed at higher levels while enhancing it near the surface. The opposite pattern is observed over the coldest SST anomalies in

385 the Amazon sub-region, where wind speed decreases near the surface and increases at and above the MABL height.

Furthermore, the warming (cooling) induced by mesoscale SST anomalies extends well above the MABL height (MABLH) (Fig. 6c). This is reflected in the two-dimensional saturation specific humidity anomaly histogram, where values exceed ± 0.1 g kg^{-1} K^{-1} in the warmest (coldest) intervals. In contrast, specific humidity variations are weaker, as suggested by the Amazon (s_q). Consistent with the Amazon s_q shown in Fig. 3, q slightly decreases over the warmest mesoscale SST

390 anomalies and slightly increases in the MABL located over the coldest SST anomalies. At the MABLH level, we find slightly positive q anomalies which then become negative further above, except for the warmest mesoscale SST anomalies. This pattern of specific humidity anomalies aligns again with the DMM: warmer SSTs destabilize the MABL leading to the entrainment of drier (and colder) air from the free troposphere towards the surface, decreasing surface q (and air temperature, thus reducing s_t with respect to Tradewind where s_q is positive as shown in Fig. 3). Consequently, the specific humidity deficit (Δq) anomalies

395 (Fig. 6e) mostly resemble those of the saturation specific humidity (q_s) in Fig. 6c, with negative Δq anomalies coinciding with negative SST anomalies, and vice versa. The only exception corresponds to the warmest mesoscale SST anomalies where negative anomalies of Δq emerge over the MABLH associated with the reduced q.

Fig. 6f presents the cloud water mixing ratio (QCLOUD). Although anomalies remain weak, an increase in QCLOUD is observed at the MABLH level for the majority of the mesoscale SST anomaly range. In regions of negative mesoscale SST

400 anomalies, the strongest QCLOUD increases are confined close to the MABLH. This finding aligns with previous observational studies, such as Acquistapace et al. (2022), which detected stratiform shallow clouds over stable tropical MABLs, and mod-
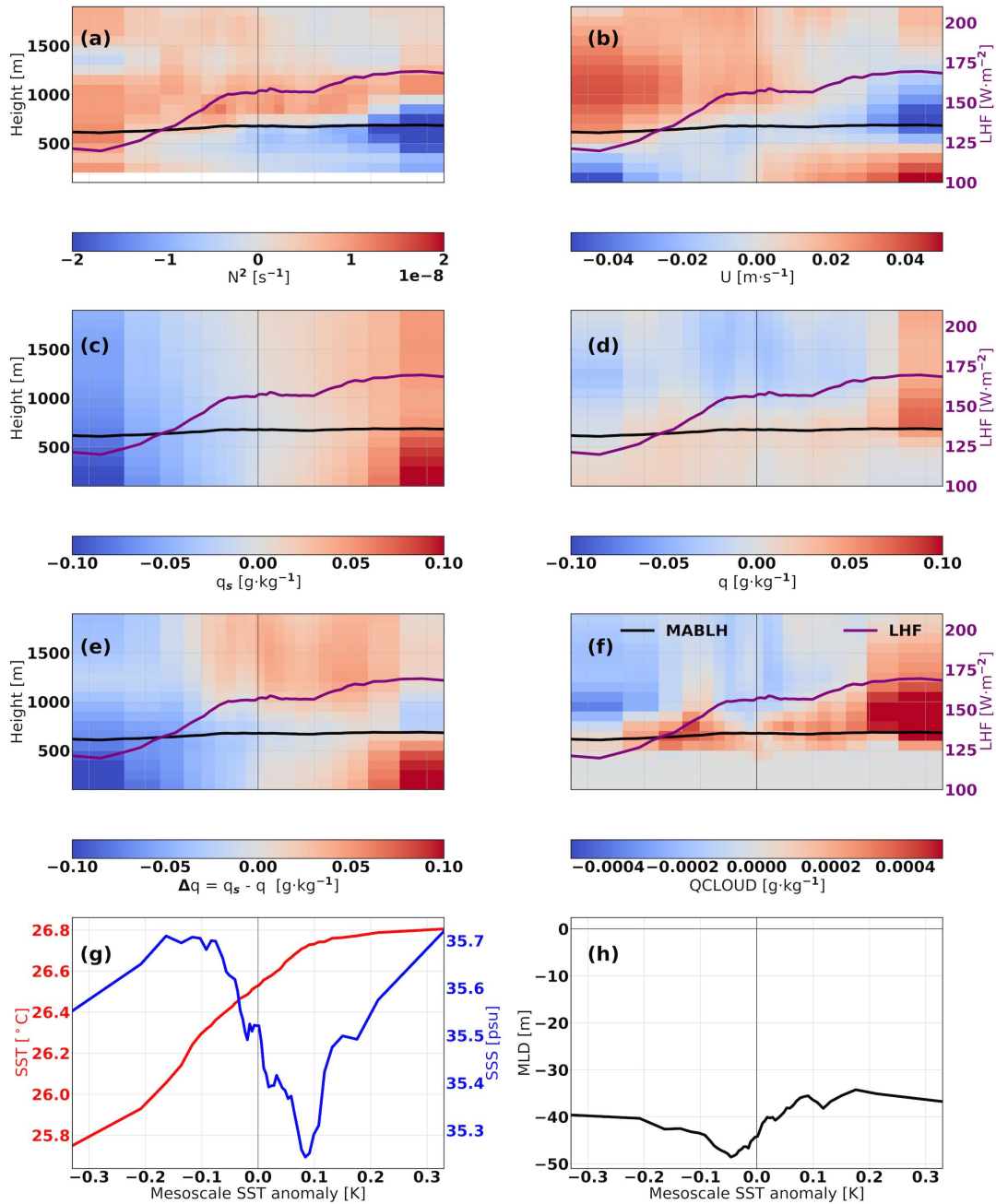
Figure 6. Panels (a)–(f) show the vertical structure of the first 2000 m of the atmosphere (in terms of mesoscale anomalies) as a function of the SST mesoscale anomaly: (a) Brunt-Väisälä frequency, (b) horizontal wind speed, (c) saturation specific humidity, (d) specific humidity, (e) specific humidity deficit, and (f) cloud water mixing ratio (QCLOUD). In all these panels, the black line represents the MABL height (MABLH), while the purple line indicates LHF. Panel (g) displays SST (red) and SSS (blue), and panel (h) shows MLD, both as functions of the SST mesoscale anomaly. All calculations are based on daily averages of the model output for JF 2020. Bins are defined using the 2% percentile range to ensure a sufficient number of values per bin.

eling studies (Borgnino et al., 2025). Over positive mesoscale SST anomalies, QCLOUD positive anomalies extend upward potentially yielding more vertically developed clouds in the context of a more unstable atmosphere.

In all the panels discussed above, the purple line represents the mean binned LHF as a function of the SST mesoscale anomaly. Consistent with observational results from both satellite (Fernández et al., 2023) and *in-situ* data (Fernández et al., 2024), a significant LHF increase of approximately 50 W m^{-2} is observed. This increase is driven by the combined effects of SST changes (thermodynamic contribution), as well as variations in specific humidity and, to a lower extent, wind speed (dynamic contribution), which were quantified separately in the previous section. Additionally, the black line represents the simulated MABLH mean per mesoscale SST anomaly bin. Its values remain around 600 m for most SST anomaly bins, consistent with expected tropical ocean conditions. A slight increase in MABLH is observed toward the warmest SSTs; however, this increase is notably weaker than that documented in *in-situ* observations by Fernández et al. (2024). Thus, the MABL response does not fully align with the downward momentum mixing (DMM) mechanism, although changes in vertical stratification, wind speed and specific humidity suggest that DMM is active at the mesoscale in the Amazon sub-region. We hypothesize that this discrepancy may arise from the MABL stability parameterizations used within the model. A more detailed analysis would be required to confirm this hypothesis, but it is beyond the scope of this study.

Note that all the anomalies (atmospheric and SST) shown in Fig. 6 are small compared to the ones shown in Borgnino et al. (2025). A direct comparison is not straightforward since their simulation is SST-forced and ours is coupled, and they use a different filtering procedure: no time filter and a high-pass Gaussian filter with a 150 km cutoff length. In addition, they evaluate the vertical atmospheric structure of the whole EURECA domain (not only Amazon). However, in the range of the anomalies presented in this article (± 0.3°C), the results are consistent. For example, in their Fig. 4d wind speed mesoscale anomalies range from -0.2 m s^{-1} to 0.2 m s^{-1} and SST mesoscale anomalies from -0.6°C to 0.5°C. Nevertheless, between ± 0.3°C their wind speed anomaly values lie within the ± 0.05 m s^{-1} range of Fig. 6b.

Finally, Figs. 6g and h illustrate the dependence of SST, SSS, and MLD on SST anomalies. SSS peaks at a mesoscale SST anomaly of -0.15°C, corresponding to the most open-ocean region of the Amazon domain. In contrast, the core of the Amazon plume, where salinity is lowest, corresponds to the warmer waters (a mesoscale SST anomaly of 0.1°C). Additionally, a relatively low SSS (~ 35.5 psu) is observed in the SST mesoscale anomaly range associated with the cold stripe waters mixing with the Amazon plume (SST mesoscale anomalies around -0.25°C). The MLD is shallowest in the core of the plume (SST mesoscale anomaly of ~ 0.1°C) and deepens toward the open ocean (between 0 and -0.1°C of SST mesoscale anomaly). Coastal waters associated with the cold SST stripe exhibit intermediate MLD values, not reaching 40 m.

We now analyze the rest of the terms of the surface heat balance (Eq. 5) in Figs. 7a and b as a function of the SST mesoscale anomaly. Here, the sign convention is inverted: positive fluxes indicate heat transfer from the atmosphere to the ocean, and vice versa. Fig. 7a reveals that the net heat flux decreases from over 50 W m^{-2} at -0.3°C SST mesoscale anomalies to negative values for anomalies above 0.2°C. This decrease is primarily driven by LHF variations and, to a lesser extent, by changes in the sensible heat flux (SHF), which declines from slightly above 0 W m^{-2} in the coldest regions to -10 W m^{-2} in the warmest bins. Note that the net radiative heat flux variations' (orange line) are smaller than those associated with LHF.
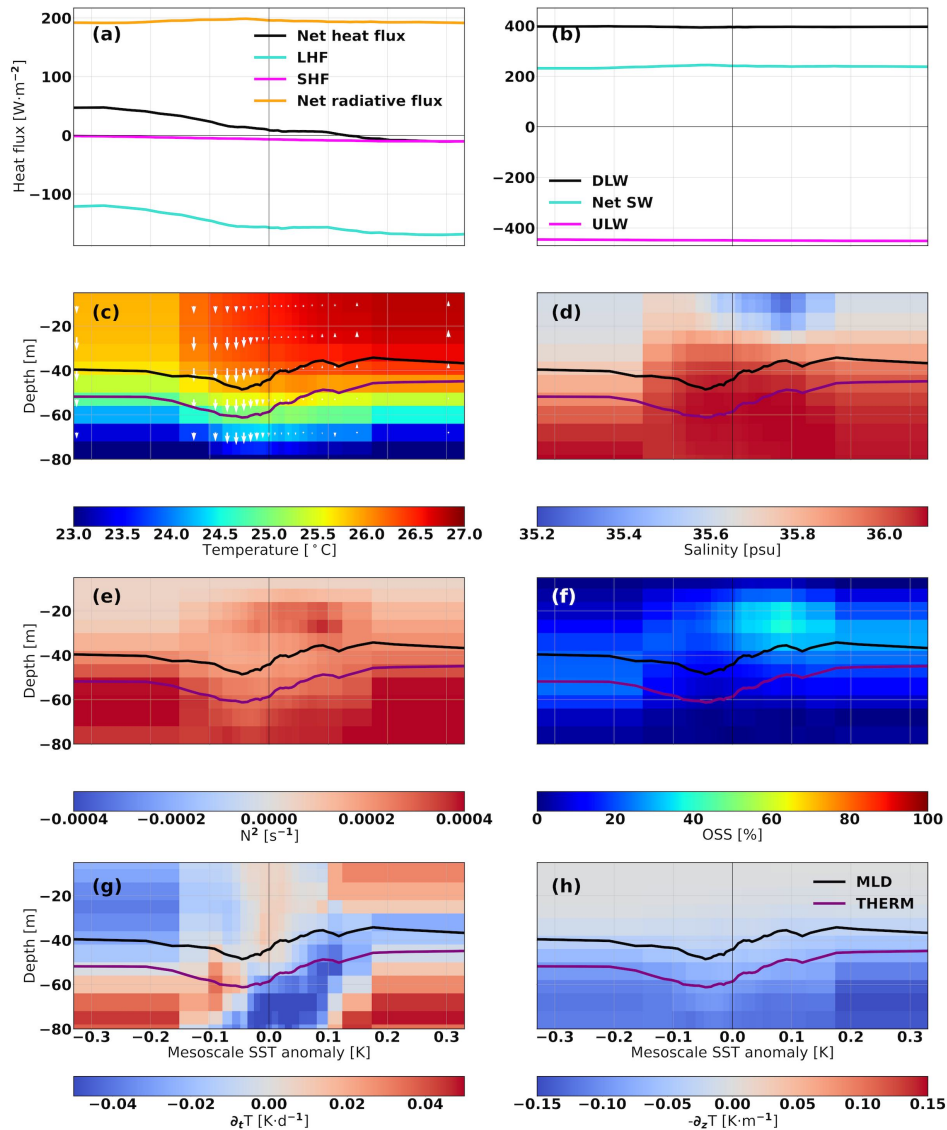
Figure 7. Behavior of various ocean properties as a function of the SST mesoscale anomaly. In (a), the black line represents the net heat flux, the turquoise line corresponds to LHF, the magenta line to SHF and the orange line the net radiative heat flux. In (b), the black line denotes downward longwave radiation, the turquoise line indicates net shortwave radiation, and the magenta line represents upward longwave radiation. Note that the sum of these three contributions yields the net radiative flux represented in orange in panel a. In both panels, the sign convention is such that positive fluxes are directed toward the ocean. Panels (c)–(h) illustrate the vertical structure of the upper 120 m of the ocean: (c) water temperature, (d) salinity, (e) Brunt-Väisälä frequency, (f) OSS index, (g) total temperature tendency, and (h) vertical temperature gradient (a negative gradient indicates decreasing temperature with depth). In these panels, the black line represents the MLD, while the purple line denotes the base of the isothermal layer. All values are based on daily model output averages for JF 2020. As in previous figures, SST anomaly bins are defined using the 2% percentile separation to ensure a sufficient number of values per bin.

We decompose the radiative heat flux contribution into its components (downward longwave radiation, shortwave radiation, and upward longwave radiation). The net shortwave heat flux remains nearly constant (cyan line in Fig. 7b), indicating a negligible impact of MABLH cloud cover changes (Fig. 6f) on air-sea heat fluxes in the Amazon sub-region. Consequently, net heat flux variations are primarily driven by turbulent heat flux (THF) modulations.

440　To gain deeper insight into the processes that govern heat redistribution within the ocean interior and their relationship with mesoscale SST anomalies, we examine the two-dimensional histograms (depth versus mesoscale SST anomaly) of several key variables in Figs. 7c–h. The warmest mesoscale anomaly SST intervals correspond to water temperatures exceeding 27°C down to the MLD, which remains around 35 m. These warmer waters are associated with low salinity values, confirming that the strongest positive mesoscale anomalies correspond to the core of the Amazon plume. Notably, enhanced vertical stratification

445　within the Amazon plume, linked to elevated Brunt-Väisälä frequency values over low-salinity waters (Fig. 7e), coincides with weak vertical motion (white arrows in Fig. 7c). Indeed, the OSS index, which quantifies the fraction of stratification attributed to salinity, indicates that salinity plays a more important role in vertical stratification. Over the core of the plume (lowest salinity and -0.1°C of mesoscale SST anomaly), OSS values reach 50%.

In contrast, the saltiest MLDs correspond to stronger vertical velocities, occurring around the mesoscale anomaly -0.1°C.

450　The coldest waters (< -0.3°C) also exhibit relatively low salinity, a signal already observed in SSS (Fig. 6g), extending throughout the ML. Despite their lower temperature, reduced salinity results in shallower MLs, weaker vertical motion, and increased stratification, particularly due to salinity effects. Fig. 7g presents the binned distribution of total temperature tendency as a function of mesoscale SST anomaly. The temperature tendency within the ML is negative for the coldest SST anomalies and positive for the Amazon plume-related bins (higher mesoscale SST anomalies), where a warming trend is observed

455　despite the net heat flux indicating heat loss from the ocean to the atmosphere (Fig. 7a). We return to this point later. Below the plume-related ML, cooling is evident, consistent with the high turbidity of plume-related waters rich in chlorophyll and nutrients (Olivier et al., 2022), which significantly reduces the amount of solar radiation reaching the MLD.

To investigate the presence of temperature inversions (observed in *in-situ* work, (Fernández et al., 2024)) and potential subsurface heat release, Fig. 7h presents the two-dimensional histogram of the vertical temperature gradient ($\partial_z T$). In general,

460　$\partial_z T$ peaks below the base of THERM (the isothermal layer computed as the depth where temperature is 0.2°C colder than SST). However, in all cases, $\partial_z T$ remains negative below the MLD, indicating a sharp decrease in temperature with depth and the absence of temperature inversions. Thus, unlike the *in-situ* observations analyzed by Fernández et al. (2024), the model fails to reproduce the temperature inversions occurring between the MLD and THERM. Consequently, their contribution to LHF spatial variability cannot be isolated.

465　To further investigate heat transfer in and out of the ML, particularly to explain why the ML undergoes net warming over plume waters despite losing heat to the atmosphere, Fig. 8 displays the various terms of the ML heat budget (Eq. 4) averaged over JF 2020. Additionally, we present the spatial distribution of MLD and the barrier layer thickness (BLT) with superimposed SST contours in Figs. 8a and b, respectively. The MLD map clearly distinguishes three water masses within the Amazon subdomain. To the west, cold waters mix with the warm and fresh Amazon plume, triggering a decoupling between haline and
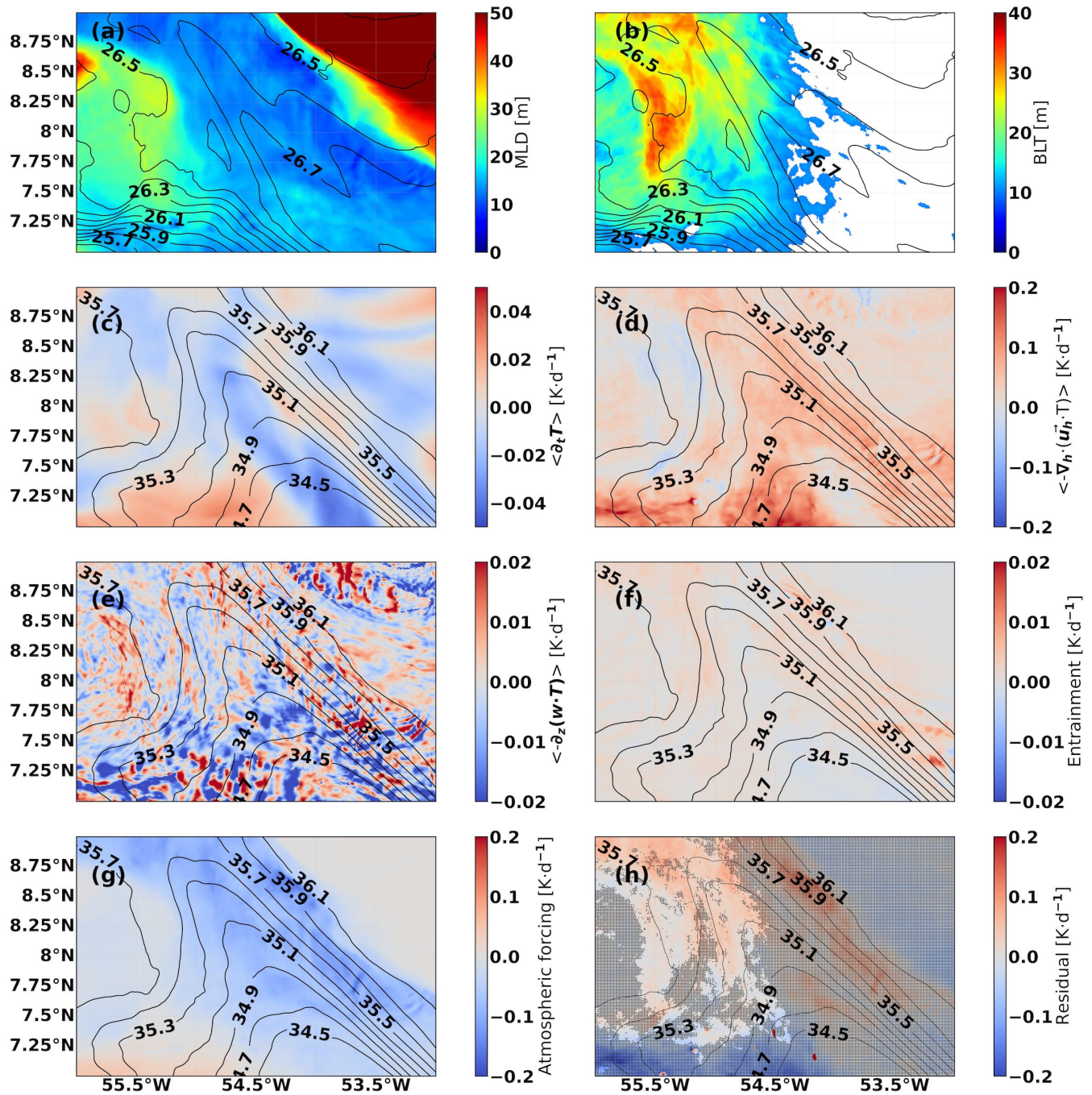
Figure 8. Averaged JF 2020 mixed layer heat budget (vertically integrated down to the mixed layer depth) for the Amazon sub-region. (a) Mean MLD and (b) mean barrier layer thickness (BLT), with black contours representing SST. Panels (c)–(h) illustrate the different terms in Eq. 4: (c) total temperature tendency, (d) horizontal advection, (e) vertical advection, (f) entrainment, (g) atmospheric forcing, and (h) residual. The hatched areas in (f) indicate locations where the residual is primarily associated with vertical diffusion, following Cronin et al. (2015).

470   thermal stratification and leading to the formation of barrier layers (BL) as thick as 35 m. In the eastern part of the domain, relatively cold and saline waters exhibit the deepest MLDs, exceeding 50 m.

The JF 2020 averaged total temperature tendency ($\partial_t T$) exhibits a highly heterogeneous pattern (Fig. 8a). In the southwestern part of the domain, warming is primarily driven by the horizontal advection of warmer waters from the south (Fig. 8b).

In contrast, the Amazon plume-related waters display a cool-warm dipole. The waters with the lowest salinity (SSS <
475   35 psu) experience net cooling, mainly due to atmospheric forcing (Fig. 8g). However, the warmest waters (SST > 26.7°C) with salinity values between 35 and 35.4 psu exhibit positive $\partial_t T$. This increase results primarily from horizontal advection, as the plume detaches from the continental shelf, and warm core waters are transported northwestward, leading to a local temperature increase. The nearly uniform temperature within the plume explains the absence of strong horizontal advection values in its interior, as warm water from the surroundings is advected into a region where little temperature variation occurs.

480   In addition to horizontal advection, entrainment contributes to the temperature tendency. Positive entrainment values are found along the 35.5 psu isoline (Fig. 8f), likely resulting from MLD variations associated with the lateral displacement of the plume. However, the magnitude of this contribution is an order of magnitude weaker than that of lateral advection. A third contributing factor is vertical diffusion. Positive values of the mixed layer heat budget residual appear around the 35.5 psu isoline (Fig. 8h). This residual can primarily be attributed to vertical diffusion, as it meets the Cronin et al. (2015) criteria used
485   in this study (detailed in Section B of the Appendix), which include the presence of a strong vertical temperature gradient, relatively weak horizontal advection at the MLD, and the absence of a barrier layer (BL, the difference between THERM and the MLD). The impact of vertical diffusion is comparable in magnitude to lateral advection. The combined effects of horizontal advection, entrainment, and vertical diffusion outweigh the cooling effect of the atmospheric forcing (Fig. 8g).

5   Discussion and Conclusion

490 High-resolution coupled simulations serve as a powerful complement to remote sensing, reanalysis, and *in-situ* observations to study ocean mesoscale influences on latent heat flux (LHF) variability in the Northwest Tropical Atlantic. In this study, we employ the WRF-CROCO coupled EURECA simulation at 1 km oceanic and 2 km atmospheric resolution, fully resolving ocean mesoscale ($O(50 - 250$ km)) processes. We focus on January–February 2020, when the Intertropical Convergence Zone (ITCZ) shifts southward, and analyze four domains: the full EURECA region; Amazon and Downstream (coastal regions, with
495 the former influenced by the Amazon plume); and Tradewind (a more quiescent open-ocean region).

Our analysis of air-sea coupling coefficients confirms a robust mesoscale positive correlation between surface current vorticity and wind curl across all regions. The associated coupling coefficient is denoted as s_w. This correlation is the strongest in the Downstream sub-region (s_w = 0.26, Fig. 3e) compared toTradewind (s_w = 0.24) and Amazon (s_w = 0.21). Although these variations might seem small, the error bars associated with these coupling coefficients do not overlap (Fig. 3, salmon
500 markers) and all s_w values are statistically significant (see Section C of the Appendix). They represent changes of 14.3% in s_w (i.e. (0.26-0.22 / 0.28)). This difference might be related to the presence of stronger surface currents in Downstream than in

Amazon and Tradewind associated with the nearly-stationary eddy located in front of Trinidad and Tobago (Fig. 2d). Stronger currents may drive a more robust wind response, less likely to be masked by other atmospheric processes.

Most coupling coefficients at the mesoscale are weaker than satellite-derived values in Fernández et al. (2023) but agree with those reported in Renault et al. (2019b). We find $s_u = 0.26$ m s^{-1} K^{-1} for the EURECA domain, peaking in Amazon and Downstream (0.29 and 0.31 m s^{-1} K^{-1} respectively, Fig. 3) and reaching its minimum in Tradewind (0.11 m s^{-1} K^{-1}, Fig. 3). This pattern reflects stronger Downward Momentum Mixing (DMM) activity in Amazon and Downstream than in Tradewind. Meanwhile, s_q is slightly negative in and Amazon Downstream (-0.05 and -0.09 g kg^{-1} K^{-1} respectively) and positive in Tradewind (0.24 g kg^{-1} K^{-1}, Fig. 3). Finally, s_t is always positive and ranges from 0.16 in Amazon (in the warm eddy corridor) to 0.25 in Tradewind (open ocean).

We quantify LHF sensitivity to sea-surface temperature (SST) anomalies through linear regression analysis (Fig. 4). Consistent with satellite observations (Fernández et al., 2023), LHF increases by 31.8% per 1°C warming, with the strongest sensitivity in Amazon (35.9% K^{-1}, Fig. 4c) and the weakest in Tradewind (25% K^{-1}, Fig. 4g). Furthermore, we separate the thermodynamic (SST-driven) and the dynamic (atmospheric response) contributions, confirming that dynamic effects dominate. The thermodynamic contribution represents only 4.5%–7% per 1°C, with specific humidity driving most dynamic LHF changes. Finally, we assess LHF sensitivity to surface currents (Fig. 5). Accounting for relative winds instead of absolute winds induces LHF variations up to 15 W m^{-2}, consistent with *in-situ* results (Fernández et al., 2024). The current feedback (CFB) effect is much smaller, contributing at most 3 W m^{-2}.

The vertical structures of the marine atmospheric boundary layer and mixed layer reveal key mechanisms behind the observed coupling. In the atmosphere, we observe DMM-consistent patterns, with a dipole in N^2 (more unstable over warm SSTs, more stable over cold SSTs) and a reduction (increase) of near-surface specific humidity (near-surface winds) over warm SST anomalies. Similar findings hold for Downstream and Tradewind (not shown). In the ocean, the warmest SST anomalies coincide with the Amazon plume core (Figs. 7c and d). They are characterized by shallower MLDs, inhibited water vertical velocity and a negative net heat flux towards the atmosphere. Despite this, positive mesoscale anomalies associated with the Amazon plume tend to continue warming ($\partial_t T > 0$) mainly because of lateral advection of warm plume-related waters, as confirmed by the mixed layer heat budget (Fig. 8).

This study extends the mesoscale findings of Fernández et al. (2023, 2024) providing a regionalized analysis of the air-sea coupling and the ocean-atmosphere vertical structure. It also links the air-sea coupling with the Amazon plume. However, our analysis is restricted to boreal winter (January and February). Future work should investigate other seasons in the EURECA simulation (June 2019–June 2020), as coupling coefficients vary seasonally (Conejero et al., 2024), with stronger air-sea interactions in boreal winter than in summer. Additionally, the Amazon runoff peaks in summer, amplifying the Amazon plume's influence on LHF heterogeneity. Moreover, this study does not address the ocean submesoscale ($O(<50$ km$)$) although evidence suggests that submesoscale ocean structures also impact the near-surface atmosphere (Meroni et al., 2018; Gaube et al., 2019). This is mainly because daily averaging, used to remove the diurnal cycle, might also eliminate important submesoscale signals. A more sophisticated approach, such as multichannel singular spectrum analysis (M-SSA), could better preserve submesoscale variability. Furthermore, comparing the higher-resolution EURECA simulation (1 km ocean, 2 km atmosphere) with

the coarser Antilles simulation (2.5 km ocean, 6 km atmosphere) would clarify the impact of spatial resolution on mesoscale and submesoscale air-sea interactions. Finally, longer simulations ($\geq$10 years) would enable interannual variability studies, particularly regarding Amazon plume detachment, which occurs irregularly (e.g., absent in 2010, 2011, and 2013; (Olivier et al., 2022)).

Our findings emphasize the need for high-resolution modeling in climate studies. Traditional climate models rely on coarse SST grids, which suppress the small-scale air-sea disequilibrium that governs LHF release. Implementing the LHF downscaling algorithm from Fernández et al. (2023) in model couplers could enhance air-sea flux representation in high-resolution climate simulations. Future work should explore its implementation within global coupled models to improve energy exchange parameterizations.

Data availability. Apart from the EURECA simulation, we benefited from several data sets made freely available and listed here.

- SeaFlux (Roberts et al., 2020), http://dx.doi.org/10.5067/SEAFLUX/DATA101

- SMAP maps produced by Remote sensing systems (RSS v4 40 km) (Boutin et al., 2021),
  https://doi.org/10.5285/5920a2c77e3c45339477acd31ce62c3c

- Global Ocean Gridded L4 Sea Surface Heights And Derived Variables Reprocessed 1993 Ongoing (CLS, 2018), https://doi.org/10.48670/moi-00148

Code and data availability. All the codes used to produce the figures of this article are available upon request to the first author.

Appendix A: Numerical Considerations in the Mixed Layer Heat Budget Computation

In the EURECA simulation, only the monthly means of the advective-diffusive equation terms are stored. For temperature, this
555   equation reads:

$$\underbrace{\partial_t \mathrm{T}}_{\text{Total tendency}} + \underbrace{\nabla \cdot (\vec{\mathrm{u}}\ \mathrm{T})}_{\text{Advection}} = \underbrace{\mathcal{F}}_{\text{Forcing}} + \underbrace{\mathcal{D}}_{\text{Mixing}} . \tag{A1}$$

One of the challenges in computing the mixed layer (ML) heat budget is ensuring its closure, as numerical choices in the calculation of each term can introduce discrepancies. To mitigate this issue, we followed the computational steps detailed in the CROCO documentation when computing all the terms in Eq. A1 on a daily basis.

560   Fig. A1 presents a comparison between the recomputed and stored Eq. A1 terms, integrated down to 100 m (a depth beyond any mixed layer depth to minimize entrainment effects). The left column (except for the last row) displays the recomputed terms, the central column shows the corresponding stored values from the simulation output, and the right column represents the numerical bias, i.e., the difference between the recomputed and stored values.

The total temperature tendency, averaged over February 2020, exhibits a consistent spatial pattern between the recomputed
565   (Fig. A1a) and stored (Fig. A1b) values. A region of strong cooling extends from the southern part of the domain (around 54°W) towards the north and northwest, surrounded by positive temperature tendency values, particularly in the southernmost part of the domain. The numerical bias (Fig. A1c) is one to two orders of magnitude smaller than the actual temperature tendency values, indicating that the numerical error in recomputing the total tendency is relatively small.

However, significant differences arise when comparing the advection terms. The recomputed horizontal (Fig. A1d) and
570   vertical (Fig. A1g) advections differ substantially in both pattern and intensity from their stored counterparts (Figs. A1e and h, respectively). The recomputed advections are systematically stronger, and their differences (Figs. A1f and i) are of the same order of magnitude as, or even exceed, the values themselves.

In contrast, the atmospheric forcing term remains consistent between the recomputed (Fig. A1j) and stored (Fig. A1k) datasets, with negligible numerical bias (Fig. A1l). This suggests that numerical errors primarily impact the advection terms,
575   while the atmospheric forcing is well represented in the recomputed dataset.

The discrepancy in the advection terms leads to a significantly large residual field (Fig. A1m), which exceeds the total temperature tendency itself (Fig. A1a). This stands in contrast to the stored residual field (Fig. A1n), where significant values are only observed around 7.5°N. The difference between the recomputed and stored residual fields (Fig. A1o) is almost as large as the recomputed residual field itself, highlighting the impact of numerical discrepancies. Additionally, the stored residual field
580   is evenly partitioned between horizontal and vertical mixing, whereas these two contributions cannot be separately estimated from the recomputed fields.

Overall, Fig. A1 underscores the critical role of numerical schemes in computing heat budgets, particularly for advection and derivative calculations. In this case, the recomputed horizontal and vertical advections were obtained using a second-order centered scheme, whereas the simulation employs a fifth-order upstream advection scheme, leading to significant differences in
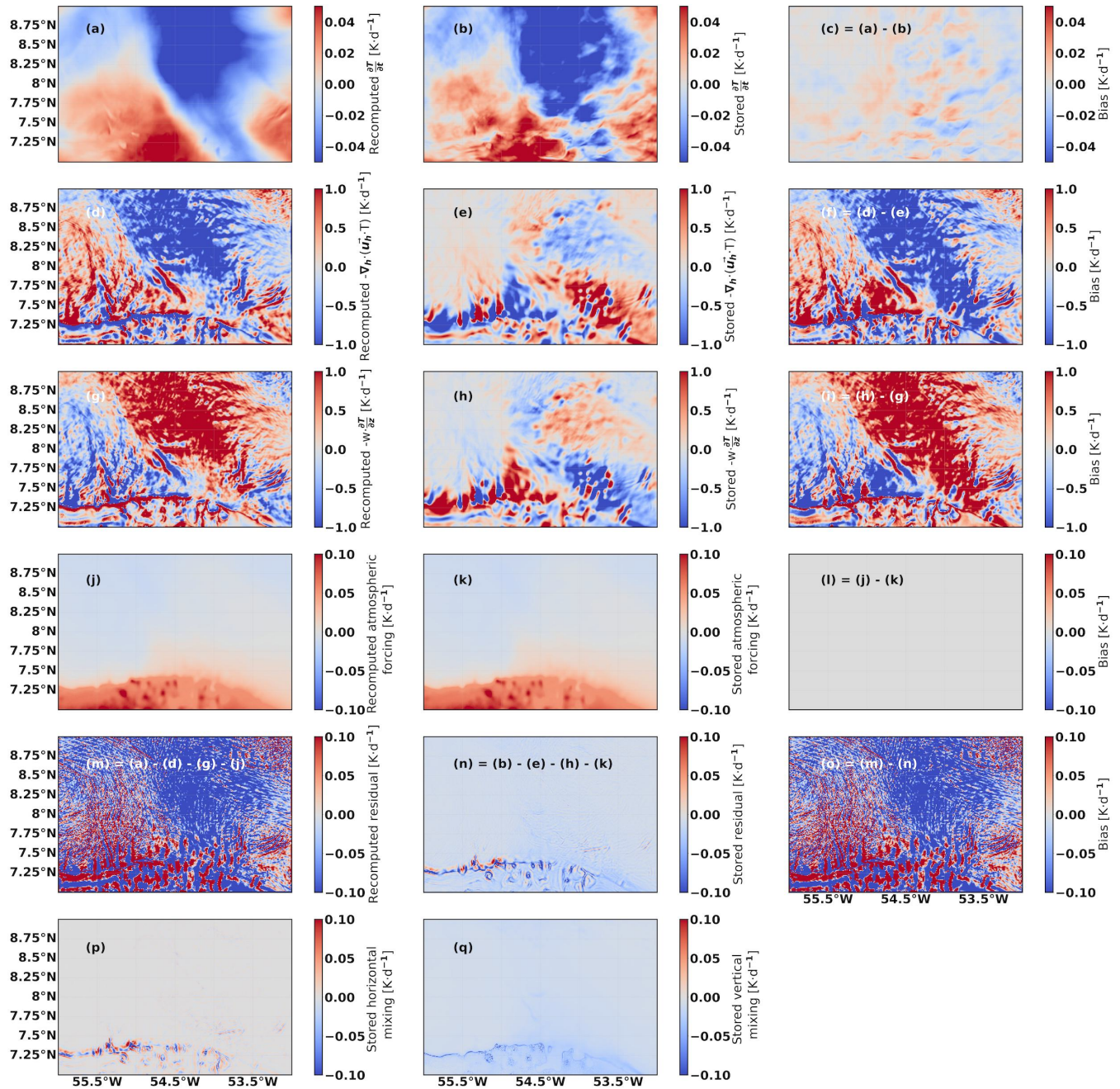
Figure A1. Comparison between the stored advective-diffusive equation terms (Eq. A1 and the recomputed ones, integrated over a layer of 100 m, (deeper than the maximum MLD recorded).

the resulting fields. Thus, in the mixed-layer heat budget-related results, we will work with the stored advection terms whereas the rest of the terms (total tendency, entrainment and atmospheric forcing) will be recomputed each day from model data and then averaged in a monthly basis.

Appendix B: Criteria to Associate the Residual from the Mixed Layer Heat Budget to Vertical Diffusion

A common approach to estimating vertical heat diffusivity is to infer it from the residual of the mixed layer heat budget (Girishkumar et al., 2020). Cronin et al. (2015) extended this approach by proposing selection criteria for estimating vertical heat diffusivity at the ML base. First, if the vertical temperature gradient is small, the residual may not be associated with vertical heat diffusivity. Therefore, we require a vertical temperature gradient greater than 0.0003 °C m^{-1} within 5 m below the MLD for the residual to be considered representative of vertical diffusion. However, as noted by Cronin et al. (2015), in the presence of strong currents, the residual term is primarily influenced by heat flux convergence in a stratified shear flow. To minimize this effect, we impose an additional filtering criterion where the residual is considered representative of vertical diffusion only when horizontal advection remains within two standard deviations of its mean value.

The formation of a barrier layer (BL) inhibits heat mixing below the ML. When the BL is thin (less than approximately 15 to 20 m), the MLD and the isothermal layer (THERM) are close to one another, typically resulting in a negative temperature gradient at the ML base. In contrast, when the BL is thick, the base of THERM is significantly deeper than the MLD, leading to a more uniform temperature profile within the BL, which can result in small temperature gradients or even temperature inversions. The barrier layer thickness (BLT) is defined as the difference between THERM and MLD when THERM is deeper than MLD (Sprintall and Tomczak, 1992). Here, we define THERM as the deepest level at which temperature decreases by at least 0.2°C relative to the 10 m-depth temperature, following Gévaudan et al. (2021). To ensure that the residual reflects vertical diffusion, we impose a final criterion: the BL must either be thinner than 15 m or contain a temperature inversion of magnitude greater than 0.2°C.

In summary:

$$\text{Residual represents vertical diffusion where} \begin{cases} \frac{\mathrm{dT}}{\mathrm{dz}} > 0.0003 \text{ °C m}^{-1} \text{ 5 m below the MLD or} \\[2mm] \nabla_\mathrm{h} \cdot (\overrightarrow{u_\mathrm{h}} \cdot \mathrm{T}) < 2 \cdot \sigma_{\nabla_\mathrm{h} \cdot (\overrightarrow{u_\mathrm{h}} \cdot \mathrm{T})} \text{ at the MLD or} \\[2mm] \mathrm{BLT} < 15 \text{ m or} \\[2mm] \mathrm{BLT} > 15 \text{ m and } \Delta\mathrm{T} > + 0.2 \text{ °C within the BL.} \end{cases} \tag{B1}$$

In the second condition, the subscript h indicates that only horizontal derivatives are considered.

Appendix C: Coupling Coefficient Linear Regressions

610 This section presents the binned linear regressions between mesoscale anomalies whose slopes are displayed in Fig. 3: the coupling coefficients. A discussion follows in Subsection 4.2.
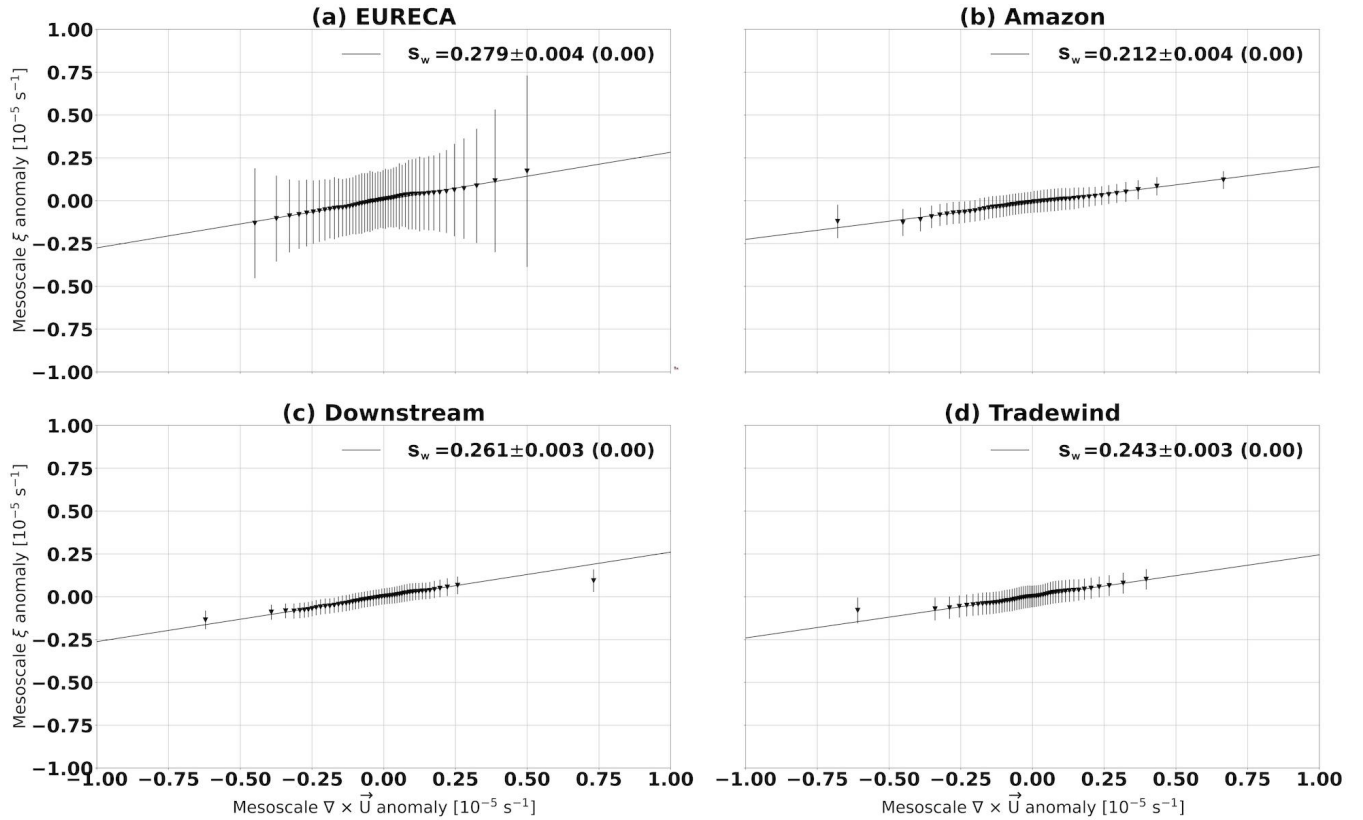

Figure C1. Binned scatter plots of surface current vorticity (ξ) versus surface wind curl mesoscale anomalies in the (a) EURECA, (b) Amazon, (c) Downstream, and (d) Tradewind. In all cases, error bars represent the standard deviation of each bin. Bins are computed using daily averages from the JF 2020 season, excluding the continental shelf (seafloor depth < 100 m) and islands as described in the main text. All the panels include least-squares regression lines for the mesoscale and submesoscale, with the slope $\pm$ standard error (p-value) indicated in the legends. To ensure a sufficiently large number of points per bin, surface current vorticity samples are divided into 2% percentile intervals, each containing at least 15 000 values.

Appendix D: Downward Momentum Mixing or Pressure Adjustment?

As mentioned in the main text, ocean mesoscale structures control the overlying surface winds through two mechanisms: Downward Momentum Mixing (DMM) (Hayes et al., 1989; Wallace et al., 1989) and Pressure Adjustment (PA) (Lindzen and
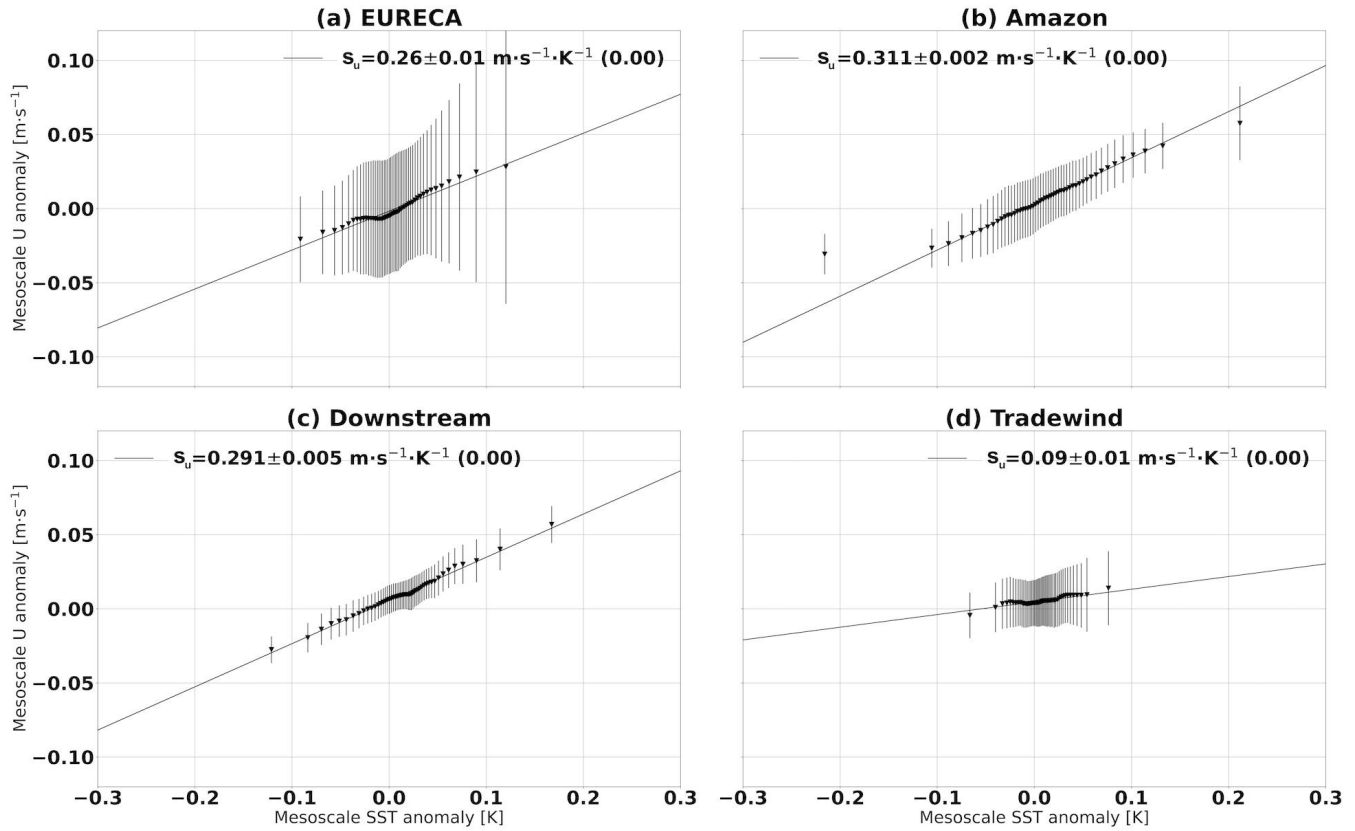
Figure C2. As in Fig. C1 but for the linear regression between near-surface wind (U) and SST mesoscale anomalies.

615   Nigam, 1987). Following the metrics introduced in (Meroni et al., 2022), we test in this section which mechanism (DMM or PA) is taking place more predominantly in EURECA, Amazon, Downstream and Tradewind so as to better understand the SST-U mesoscale coupling. If the PA mechanism is active, positive correlations between surface wind divergence and the SST Laplacian field, both computed in the direction orthogonal to the large-scale wind are expected. In turn, the presence of DMM implies a positive correlation between the wind divergence along the large-scale wind direction and the along-wind SST

620   gradient, computed as the scalar product of the SST gradient and the large-scale wind vector.

Fig. D1 shows the binned scatter plot of the along-wind wind divergence against the along-wind SST gradient mesoscale anomalies for EURECA (Fig. D1a), Amazon (Fig. D1b), Downstream (Fig. D1c) and Tradewind (Fig. D1d). In all the cases, the along-wind wind divergence increases with the along-wind wind SST gradient mesoscale anomalies at a rate of 0.5 m s^{-1} K^{-1} in EURECA which peaks at 0.55 m s^{-1} K^{-1} in Tradewind and decreases to 0.32 m s^{-1} K^{-1} in Amazon. All the slope values

625   are statistically significant at the 99% level after a two-sided t-test as indicated by the p-values in parenthesis. Thus DMM is significantly acting in the modulation of the surface wind field in all the EURECA and the three sub-regions.
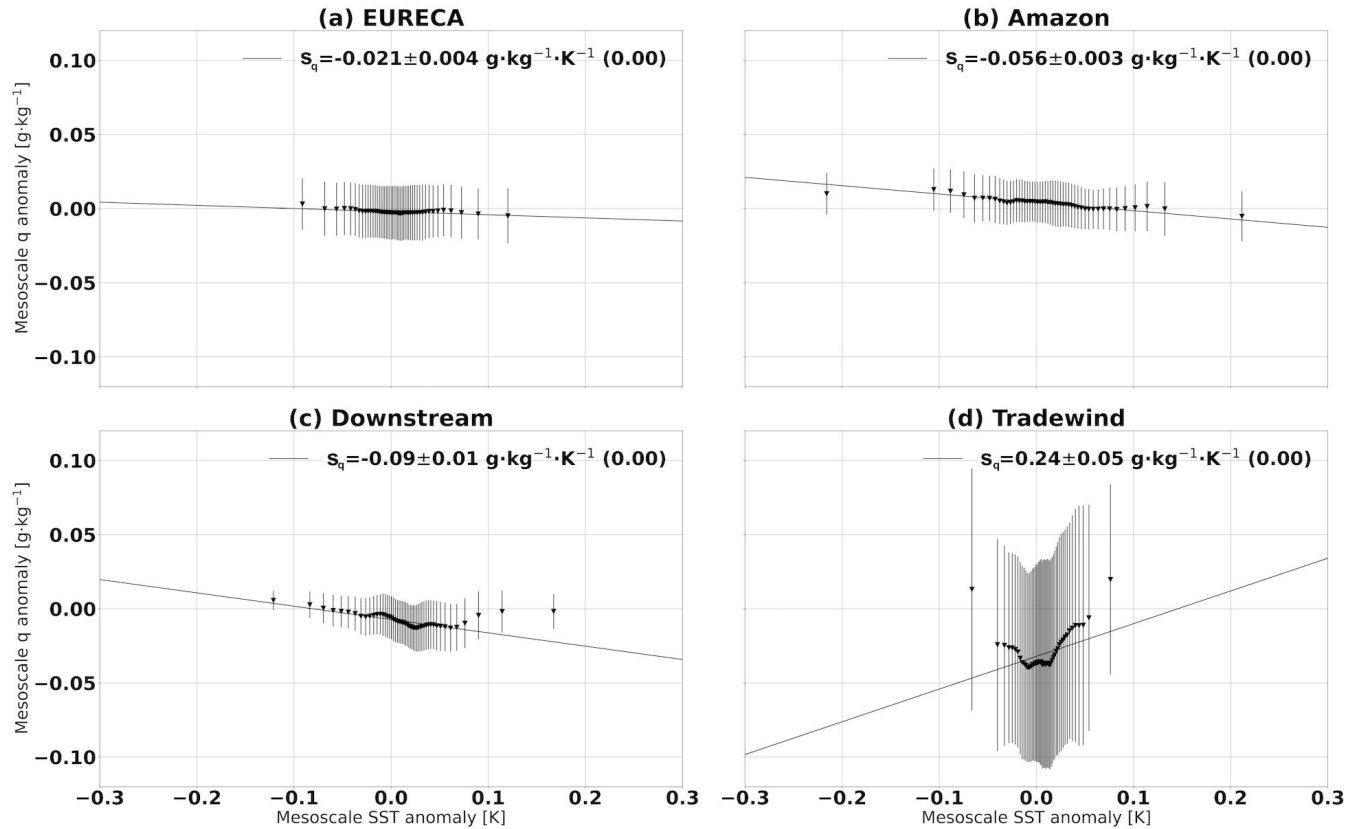
Figure C3. As in Figs. C1 and C2 but for the linear regression between near-surface specific humidity (q) and SST mesoscale anomalies.

On the other hand, Fig m D2 displays the binned scatter plot of the across-wind wind divergence against the across-wind SST Laplacian mesoscale anomalies for EURECA (Fig. D1a), Amazon (Fig. D1b), Downstream (Fig. D1c) and Tradewind (Fig. D1d). In EURECA, the slope is negative (and the p-value exceeds 0.01) suggesting that PA is not significant when con-
630 sidering the EURECA region as a whole. The same result was obtained by (Fernández et al., 2023) using satellite observations. The same applies to Tradewind. However, in the warm eddy corridor (Amazon and Downstream), the slopes are positive. This means that PA is acting together with DMM in driving surface wind mesoscale variations. This is, perhaps one of the reasons why we observe such weak wind speed anomalies in Fig. 6b (together with the weak SST anomalies when compared to satellite observations (Fernández et al., 2023) or SST-forced atmospheric simulations (Borgnino et al., 2025) in the same region).
635 However, DMM seems to dominate, as the wind speed vertical and stratification mesoscale anomaly vertical structures are consistent with it.
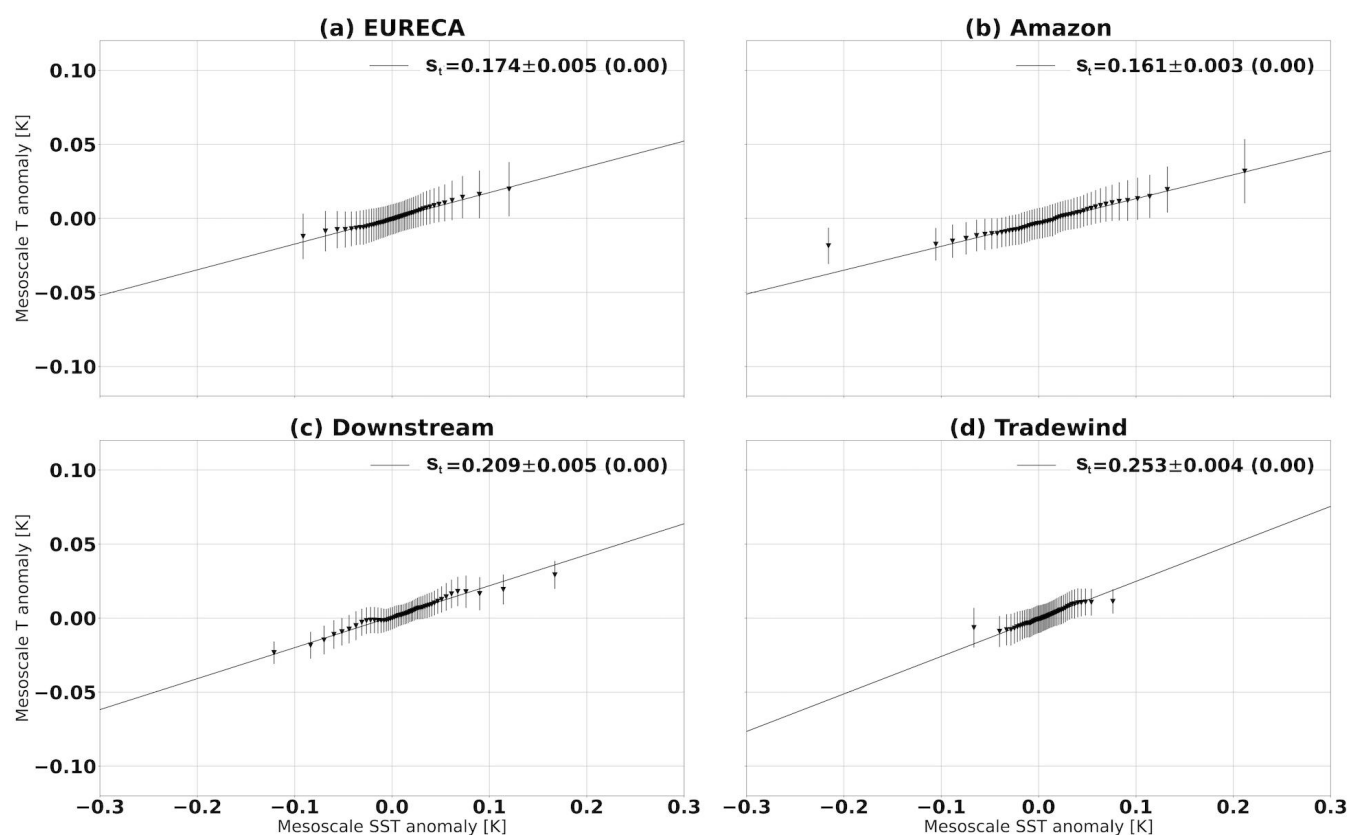
Figure C4. As in Figs. C1, C2 and C3 but for the linear regression between near-surface temperature (T) and SST mesoscale anomalies.
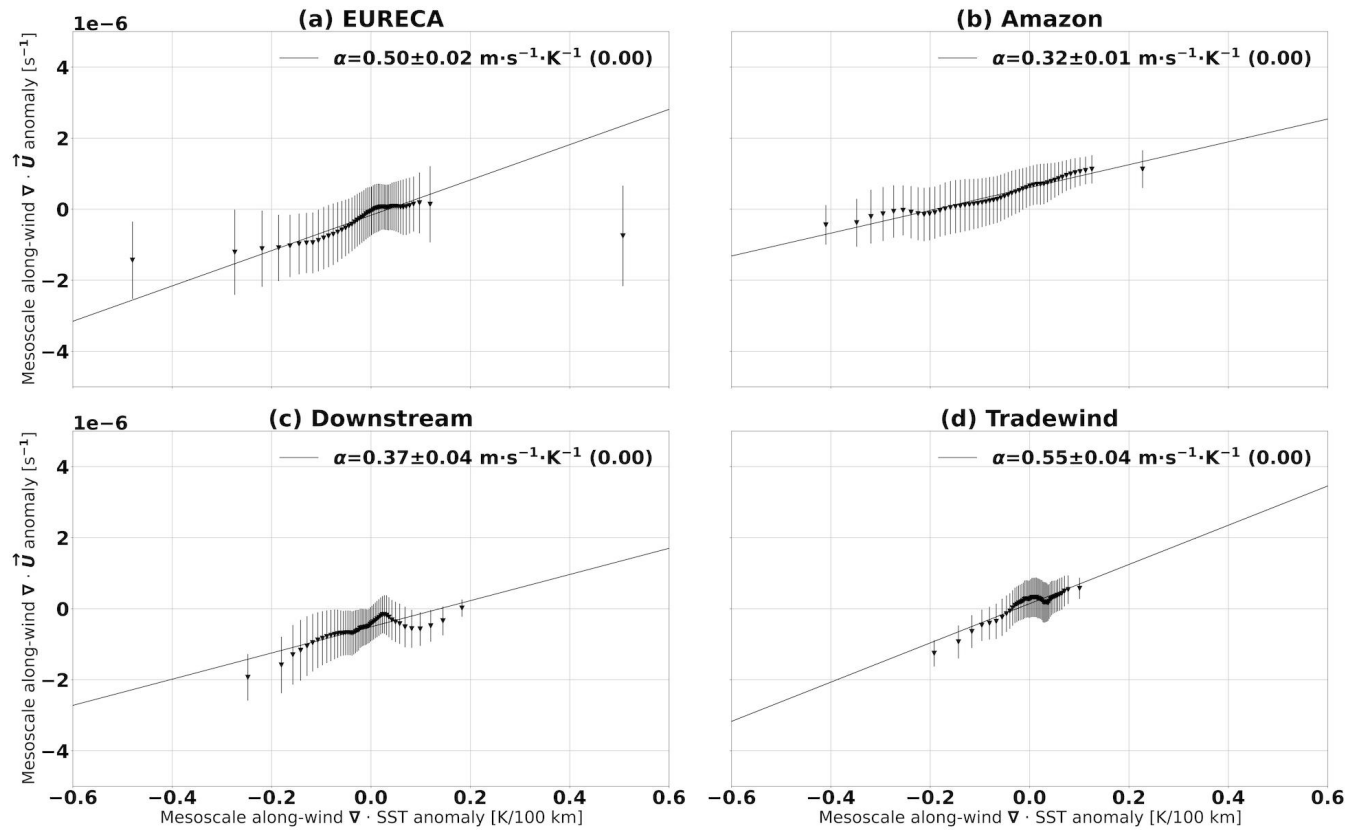
Figure D1. Binned scatter plots of the along-wind SST gradient (ξ) versus the along-wind wind divergence mesoscale anomalies in the (a) EURECA, (b) Amazon, (c) Downstream, and (d) Tradewind. In all cases, error bars represent the standard deviation of each bin. Bins are computed using daily averages from the JF 2020 season, excluding the continental shelf (seafloor depth < 100 m) and islands as described in the main text. All the panels include least-squares regression lines for the mesoscale and submesoscale, with the slope $\pm$ standard error (p-value) indicated in the legends. To ensure a sufficiently large number of points per bin, surface current vorticity samples are divided into 2% percentile intervals, each containing at least 15 000 values.
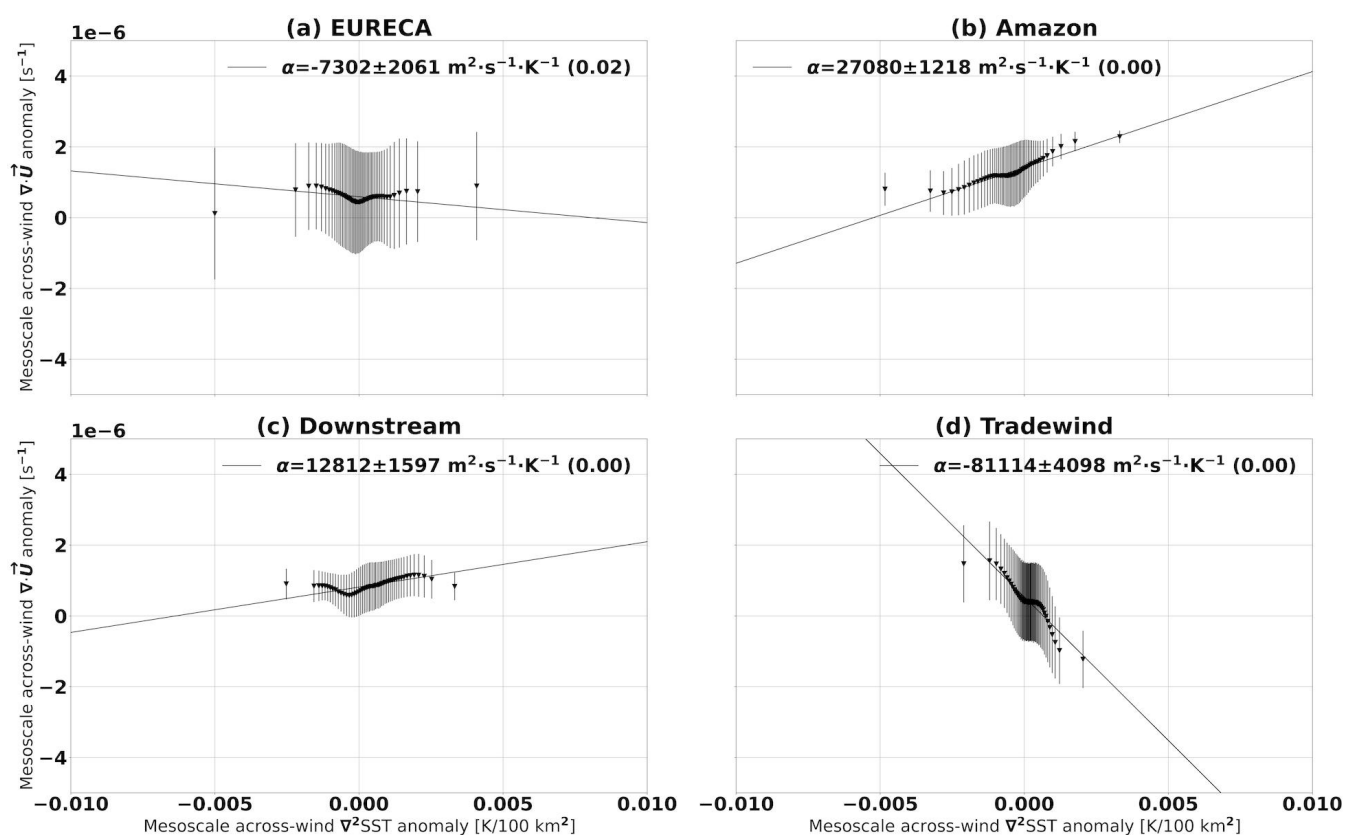
Figure D2. Like in Fig. D1 but for the across-wind SST Laplacian versus the across-wind wind divergence mesoscale anomalies.

Author contributions. All authors contributed to the conception and design of the study. CC and LR conducted the EURECA simulation, while PF and SS performed the analyses using its output. These analyses benefited from the contributions of CC, LR, FD, CP and GL. GL provided technical support with the computing tools required for processing the model data as well. PF drafted the initial version of the manuscript, and all authors approved the final submitted version.

Competing interests. The authors declare that the research was conducted without any commercial or financial relationships that could be construed as a potential conflict of interest.

References

Acquistapace, C., Meroni, A. N., Labbri, G., Lange, D., Späth, F., Abbas, S., and Bellenger, H.: Fast atmospheric response to a cold oceanic
    mesoscale patch in the north-western tropical Atlantic, Journal of Geophysical Research: Atmospheres, 127, e2022JD036 799, 2022.

Anderson, L. A., McGillicuddy Jr, D. J., Maltrud, M. E., Lima, I. D., and Doney, S. C.: Impact of eddy–wind interaction on eddy demograph-
    ics and phytoplankton community structure in a model of the North Atlantic Ocean, Dynamics of Atmospheres and Oceans, 52, 80–94,
    2011.

Anderson, S. P., Weller, R. A., and Lukas, R. B.: Surface buoyancy forcing and the mixed layer of the western Pacific warm pool: Observations
    and 1D model results, Journal of Climate, 9, 3056–3085, 1996.

Balaguru, K., Chang, P., Saravanan, R., Leung, L. R., Xu, Z., Li, M., and Hsieh, J.-S.: Ocean barrier layers' effect on tropical cyclone
    intensification, Proceedings of the National Academy of Sciences, 109, 14 343–14 347, 2012.

Bishop, S. P., Small, R. J., Bryan, F. O., and Tomas, R. A.: Scale-dependence of midlatitude air-sea interaction, Journal of Climate, 30,
    8207–8221, https://doi.org/10.1175/JCLI-D-17-0159.1, 2017.

Borgnino, M., Desbiolles, F., Meroni, A. N., and Pasquero, C.: Lower Tropospheric Response to Local Sea Surface Temperature Anomalies:
    A Numerical Study in the EUREC^{4}A Region, Geophys. Res. Lett., 2025.

Boutin, J., Vergely, J., Reul, N., Catany, R., Koehler, J., Martin, A., Rouffi, F., Arias, M., Chakroun, M., Corato, G., et al.: ESA Sea Surface
    Salinity Climate Change Initiative (Sea_Surface_Salinity_cci): weekly and monthly sea surface salinity products, v03. 21, for 2010 to
    2020 [Dataset]. CEDA., https://doi.org/https://dx.doi.org/10.5285/5920a2c77e3c45339477acd31ce62c3c, 2021.

Breugem, W.-P., Chang, P., Jang, C., Mignot, J., and Hazeleger, W.: Barrier layers and tropical Atlantic SST biases in coupled GCMs, Tellus
    A: Dynamic Meteorology and Oceanography, 60, 885–897, 2008.

Bye, J. A.: Large-scale momentum exchange in the coupled atmosphere-ocean, in: Elsevier oceanography series, vol. 40, pp. 51–61, Elsevier,
    1985.

Chelton, D. and Xie, S.: Coupled atmosphere–ocean interactions at ocean mesoscales, Oceanography, 23, 52–69, 2010.

Chelton, D. B., Esbensen, S. K., Schlax, M. G., Thum, N., Freilich, M. H., Wentz, F. J., Gentemann, C. L., McPhaden, M. J., and Schopf,
    P. S.: Observations of coupling between surface wind stress and sea surface temperature in the eastern tropical Pacific, Journal of Climate,
    14, 1479–1498, 2001.

Chelton, D. B., Schlax, M. G., and Samelson, R. M.: Summertime coupling between sea surface temperature and wind stress in the California
    Current System, Journal of Physical Oceanography, 37, 495–517, 2007.

Chen, L., Jia, Y., and Liu, Q.: Oceanic eddy-driven atmospheric secondary circulation in the winter Kuroshio Extension region, Journal of
    Oceanography, 73, 295–307, 2017.

CLS: Global Ocean Gridded L 4 Sea Surface Heights And Derived Variables Reprocessed 1993 Ongoing [Dataset],
    https://doi.org/https://doi.org/10.48670/moi-00148, 2018.

Coadou-Chaventon, S., Speich, S., Zhang, D., Rocha, C. B., and Swart, S.: Oceanic fronts driven by the Amazon freshwater plume and their
    thermohaline compensation at the submesoscale, Journal of Geophysical Research: Oceans, 129, e2024JC021 326, 2024.

Conejero, C., Renault, L., Desbiolles, F., McWilliams, J., and Giordani, H.: Near-Surface Atmospheric Response to Meso-and Submesoscale
    Current and Thermal Feedbacks, Journal of Physical Oceanography, 54, 823–848, 2024.

Conejero, C., Renault, L., Desbiolles, F., and Giordani, H.: Unveiling the Influence of the Daily Oceanic (Sub) Mesoscale Thermal Feedback
    to the Atmosphere, Journal of Physical Oceanography, 2025.

685 Craig, A., Valcke, S., and Coquart, L.: Development and performance of a new version of the OASIS coupler, OASIS3-MCT_3. 0, Geoscientific Model Development, 10, 3297–3308, 2017.

Cronin, M. F., Pelland, N. A., Emerson, S. R., and Crawford, W. R.: Estimating diffusivity from the mixed layer heat and salt balances in the N orth P acific, Journal of Geophysical Research: Oceans, 120, 7346–7362, 2015.

de Boyer Montégut, C., Mignot, J., Lazar, A., and Cravatte, S.: Control of salinity on the mixed layer depth in the world ocean: 1. General
690 description, Journal of Geophysical Research: Oceans, 112, 2007.

Debreu, L., Marchesiello, P., Penven, P., and Cambon, G.: Two-way nesting in split-explicit ocean models: Algorithms, implementation and validation, Ocean Modelling, 49, 1–21, 2012.

Desbiolles, F., Blanke, B., Bentamy, A., and Grima, N.: Origin of fine-scale wind stress curl structures in the Benguela and Canary upwelling systems, Journal of Geophysical Research: Oceans, 119, 7931–7948, 2014.

695 Desbiolles, F., Meroni, A. N., Renault, L., and Pasquero, C.: Environmental control of wind response to sea surface temperature patterns in reanalysis dataset, Journal of Climate, 36, 3881–3893, 2023.

Dewar, W. K. and Flierl, G. R.: Some effects of the wind on rings, Journal of physical oceanography, 17, 1653–1667, 1987.

Eden, C. and Dietze, H.: Effects of mesoscale eddy/wind interactions on biological new production and eddy kinetic energy, Journal of Geophysical Research: Oceans, 114, 2009.

700 Edson, J. B., Jampana, V., Weller, R. A., Bigorre, S. P., Plueddemann, A. J., Fairall, C. W., Miller, S. D., Mahrt, L., Vickers, D., and Hersbach, H.: On the exchange of momentum over the open ocean, Journal of Physical Oceanography, 43, 1589–1610, 2013.

Fairall, C. W., Bradley, E. F., Hare, J., Grachev, A. A., and Edson, J. B.: Bulk parameterization of air–sea fluxes: Updates and verification for the COARE algorithm, Journal of climate, 16, 571–591, 2003.

Fernández, P., Speich, S., Borgnino, M., Meroni, A. N., Desbiolles, F., and Pasquero, C.: On the importance of the atmospheric coupling to
705 the small-scale ocean in the modulation of latent heat flux, Frontiers in Marine Science, 10, 1136 558, 2023.

Fernández, P., Speich, S., Bellenger, H., Lange Vega, D., Karstensen, J., Zhang, D., and Rocha, C. B.: On the mechanisms driving latent heat flux variations in the Northwest Tropical Atlantic, Journal of Geophysical Research: Oceans, 129, e2023JC020 658, 2024.

Foltz, G. R. and McPhaden, M. J.: Impact of barrier layer thickness on SST in the central tropical North Atlantic, Journal of Climate, 22, 285–299, 2009.

710 Foussard, A., Lapeyre, G., and Plougonven, R.: Response of surface wind divergence to mesoscale SST anomalies under different wind conditions, Journal of the Atmospheric Sciences, 76, 2065–2082, 2019.

Fratantoni, D. M. and Glickson, D. A.: North Brazil Current ring generation and evolution observed with SeaWiFS, Journal of Physical Oceanography, 32, 1058–1074, 2002.

Gaube, P., Chelton, D. B., Strutton, P. G., and Behrenfeld, M. J.: Satellite observations of chlorophyll, phytoplankton biomass, and Ekman
715 pumping in nonlinear mesoscale eddies, Journal of Geophysical Research: Oceans, 118, 6349–6370, 2013.

Gaube, P., Chelton, D. B., Samelson, R. M., Schlax, M. G., and O'Neill, L. W.: Satellite observations of mesoscale eddy-induced Ekman pumping, Journal of Physical Oceanography, 45, 104–132, 2015.

Gaube, P., Chickadel, C., Branch, R., and Jessup, A.: Satellite observations of SST-induced wind speed perturbation at the oceanic submesoscale, Geophysical Research Letters, 46, 2690–2695, 2019.

720 Gentemann, C. L., Clayson, C. A., Brown, S., Lee, T., Parfitt, R., Farrar, J. T., Bourassa, M., Minnett, P. J., Seo, H., Gille, S. T., et al.: FluxSat: measuring the ocean–atmosphere turbulent exchange of heat and moisture from space, Remote Sensing, 12, 1796, 2020.

Gévaudan, M., Jouanno, J., Durand, F., Morvan, G., Renault, L., and Samson, G.: Influence of ocean salinity stratification on the tropical
    Atlantic Ocean surface, Climate Dynamics, 57, 321–340, 2021.

Gill, A. E. and Adrian, E.: Atmosphere-ocean dynamics, vol. 30, Academic press, 1982.

725 Girishkumar, M., Ashin, K., McPhaden, M., Balaji, B., and Praveenkumar, B.: Estimation of vertical heat diffusivity at the base of the mixed
    layer in the Bay of Bengal, Journal of Geophysical Research: Oceans, 125, e2019JC015 402, 2020.

Gruber, N., Lachkar, Z., Frenzel, H., Marchesiello, P., Münnich, M., McWilliams, J. C., Nagai, T., and Plattner, G.-K.: Eddy-induced reduc-
    tion of biological production in eastern boundary upwelling systems, Nature geoscience, 4, 787–792, 2011.

Hayes, S., McPhaden, M., and Wallace, J.: The influence of sea-surface temperature on surface wind in the eastern equatorial Pacific: Weekly
730   to monthly variability, Journal of Climate, 2, 1500–1506, 1989.

Hernandez, O., Jouanno, J., and Durand, F.: Do the Amazon and Orinoco freshwater plumes really matter for hurricane-induced ocean surface
    cooling?, Journal of Geophysical Research: Oceans, 121, 2119–2141, 2016.

Iyer, S., Drushka, K., Thompson, E. J., and Thomson, J.: Small-scale spatial variations of air-sea heat, moisture, and buoyancy fluxes in the
    tropical trade winds, Journal of Geophysical Research: Oceans, 127, e2022JC018 972, 2022.

735 Johns, W. E., Lee, T. N., Schott, F. A., Zantopp, R. J., and Evans, R. H.: The North Brazil Current retroflection: Seasonal structure and eddy
    variability, Journal of Geophysical Research: Oceans, 95, 22 103–22 120, 1990.

Krishnamohan, K., Vialard, J., Lengaigne, M., Masson, S., Samson, G., Pous, S., Neetu, S., Durand, F., Shenoi, S., and Madec, G.: Is there
    an effect of Bay of Bengal salinity on the northern Indian Ocean climatological rainfall?, Deep Sea Research Part II: Topical Studies in
    Oceanography, 166, 19–33, 2019.

740 Leyba, I. M., Saraceno, M., and Solman, S. A.: Air-sea heat fluxes associated to mesoscale eddies in the Southwestern Atlantic Ocean and
    their dependence on different regional conditions, Climate Dynamics, 49, 2491–2501, 2017.

Lindzen, R. S. and Nigam, S.: On the role of sea surface temperature gradients in forcing low-level winds and convergence in the tropics,
    Journal of Atmospheric Sciences, 44, 2418–2436, 1987.

Liu, H., Li, W., Chen, S., Fang, R., and Li, Z.: Atmospheric response to mesoscale ocean eddies over the South China Sea, Advances in
745   Atmospheric Sciences, 35, 1189–1204, 2018.

Liu, Y., Yu, L., and Chen, G.: Characterization of sea surface temperature and air-sea heat flux anomalies associated with mesoscale eddies
    in the South China Sea, Journal of Geophysical Research: Oceans, 125, e2019JC015 470, 2020.

Ma, J., Xu, H., Dong, C., Lin, P., and Liu, Y.: Atmospheric responses to oceanic eddies in the Kuroshio Extension region, Journal of
    Geophysical Research: Atmospheres, 120, 6313–6330, 2015.

750 Ma, Z., Fei, J., Lin, Y., and Huang, X.: Modulation of clouds and rainfall by tropical cyclone's cold wakes, Geophysical Research Letters,
    47, e2020GL088 873, 2020.

Maes, C. and O'Kane, T. J.: Seasonal variations of the upper ocean salinity stratification in the Tropics, Journal of Geophysical Research:
    Oceans, 119, 1706–1722, 2014.

Mahadevan, A., Jaeger, G. S., Freilich, M., Omand, M. M., Shroyer, E. L., and Sengupta, D.: Freshwater in the Bay of Bengal: Its fate and
755   role in air-sea heat exchange, Oceanography, 29, 72–81, 2016.

Martin, A. P. and Richards, K. J.: Mechanisms for vertical nutrient transport within a North Atlantic mesoscale eddy, Deep Sea Research Part
    II: Topical Studies in Oceanography, 48, 757–773, 2001.

Meroni, A. N., Parodi, A., and Pasquero, C.: Role of SST patterns on surface wind modulation of a heavy midlatitude precipitation event,
    Journal of Geophysical Research: Atmospheres, 123, 9081–9096, 2018.

760   Meroni, A. N., Giurato, M., Ragone, F., and Pasquero, C.: Observational evidence of the preferential occurrence of wind convergence over sea surface temperature fronts in the Mediterranean, Quarterly Journal of the Royal Meteorological Society, 146, 1443–1458, 2020.

Meroni, A. N., Desbiolles, F., and Pasquero, C.: Introducing New Metrics for the Atmospheric Pressure Adjustment to Thermal Structures at the Ocean Surface, J. Geophys. Res.: Atmospheres, 2022.

Mignot, J., Lazar, A., and Lacarra, M.: On the formation of barrier layers and associated vertical temperature inversions: A focus on the
765   northwestern tropical Atlantic, Journal of Geophysical Research: Oceans, 117, 2012.

Miller, J. R.: The salinity effect in a mixed layer ocean model, Journal of Physical Oceanography, 6, 29–35, 1976.

Minobe, S., Kuwano-Yoshida, A., Komori, N., Xie, S.-P., and Small, R. J.: Influence of the Gulf Stream on the troposphere, Nature, 452, 206–209, 2008.

Nagai, T., Gruber, N., Frenzel, H., Lachkar, Z., McWilliams, J. C., and Plattner, G.-K.: Dominant role of eddies and filaments in the offshore
770   transport of carbon and nutrients in the C alifornia C urrent S ystem, Journal of Geophysical Research: Oceans, 120, 5318–5341, 2015.

Oerder, V., Colas, F., Echevin, V., Masson, S., and Lemarié, F.: Impacts of the mesoscale ocean-atmosphere coupling on the Peru-Chile ocean dynamics: The current-induced wind stress modulation, Journal of Geophysical Research: Oceans, 123, 812–833, 2018.

Olivier, L., Boutin, J., Reverdin, G., Lefèvre, N., Landschützer, P., Speich, S., Karstensen, J., Labaste, M., Noisel, C., Ritschel, M., et al.: Wintertime process study of the North Brazil Current rings reveals the region as a larger sink for CO 2 than expected, Biogeosciences, 19,
775   2969–2988, 2022.

O'Neill, L. W., Chelton, D. B., Esbensen, S. K., and Wentz, F. J.: High-resolution satellite measurements of the atmospheric boundary layer response to SST variations along the Agulhas Return Current, Journal of Climate, 18, 2706–2723, 2005.

Pailler, K., Bourles, B., and Gouriou, Y.: The barrier layer in the western tropical Atlantic Ocean, Geophysical Research Letters, 26, 2069–2072, 1999.

780   Pasquero, C., Desbiolles, F., and Meroni, A. N.: Air-sea interactions in the cold wakes of tropical cyclones, Geophysical Research Letters, 48, e2020GL091 185, 2021.

Renault, L., Deutsch, C., McWilliams, J. C., Frenzel, H., Liang, J.-H., and Colas, F.: Partial decoupling of primary productivity from upwelling in the California Current system, Nature Geoscience, 9, 505–508, 2016a.

Renault, L., Molemaker, M. J., McWilliams, J. C., Shchepetkin, A. F., Lemarié, F., Chelton, D., Illig, S., and Hall, A.: Modulation of wind
785   work by oceanic current interaction with the atmosphere, Journal of Physical Oceanography, 46, 1685–1704, 2016b.

Renault, L., Lemarié, F., and Arsouze, T.: On the implementation and consequences of the oceanic currents feedback in ocean–atmosphere coupled models, Ocean Modelling, 141, 101 423, 2019a.

Renault, L., Masson, S., Oerder, V., Jullien, S., and Colas, F.: Disentangling the mesoscale ocean-atmosphere interactions, Journal of Geophysical Research: Oceans, 124, 2164–2178, 2019b.

790   Renault, L., Masson, S., Oerder, V., Colas, F., and McWilliams, J.: Modulation of the oceanic mesoscale activity by the mesoscale thermal feedback to the atmosphere, Journal of Physical Oceanography, 53, 1651–1667, 2023.

Reverdin, G., Olivier, L., Foltz, G., Speich, S., Karstensen, J., Horstmann, J., Zhang, D., Laxenaire, R., Carton, X., Branger, H., et al.: Formation and evolution of a freshwater plume in the northwestern tropical Atlantic in February 2020, Journal of Geophysical Research: Oceans, 126, e2020JC016 981, 2021.

795   Richardson, P., Hufford, G., Limeburner, R., and Brown, W.: North Brazil current retroflection eddies, Journal of Geophysical Research: Oceans, 99, 5081–5093, 1994.

Roberts, J. B., Clayson, C. A., and Robertson, F. R.: Seaflux Data Products V3 [Dataset] Earthdata, 2020.

Shchepetkin, A. F. and McWilliams, J. C.: The regional oceanic modeling system (ROMS): a split-explicit, free-surface, topography-following-coordinate oceanic model, Ocean modelling, 9, 347–404, 2005.

800 Skamarock, W. C., Klemp, J. B., Dudhia, J., Gill, D. O., Barker, D. M., Duda, M. G., Huang, X.-Y., Wang, W., Powers, J. G., et al.: A description of the advanced research WRF version 3, NCAR technical note, 475, 10–5065, 2008.

Small, R. J., DeSzoeke, S. P., Xie, S. P., O'Neill, L., Seo, H., Song, Q., Cornillon, P., Spall, M., and Minobe, S.: Air-sea interaction over ocean fronts and eddies, Dynamics of Atmospheres and Oceans, 45, 274–319, 2008.

Small, R. J., Bryan, F. O., Bishop, S. P., and Tomas, R. A.: Air–sea turbulent heat fluxes in climate models and observational analyses: What
805 drives their variability?, Journal of Climate, 32, 2397–2421, 2019.

Sprintall, J. and Tomczak, M.: Evidence of the barrier layer in the surface layer of the tropics, Journal of Geophysical Research: Oceans, 97, 7305–7316, 1992.

Vialard, J. and Delecluse, P.: An OGCM study for the TOGA decade. Part I: Role of salinity in the physics of the western Pacific fresh pool, Journal of Physical Oceanography, 28, 1071–1088, 1998.

810 Villas Bôas, A., Sato, O., Chaigneau, A., and Castelão, G.: The signature of mesoscale eddies on the air-sea turbulent heat fluxes in the South Atlantic Ocean, Geophysical Research Letters, 42, 1856–1862, 2015.

Wallace, J. M., Mitchell, T., and Deser, C.: The influence of sea-surface temperature on surface wind in the eastern equatorial Pacific: Seasonal and interannual variability, Journal of Climate, 2, 1492–1499, 1989.

Xu, H., Xu, M., Xie, S.-P., and Wang, Y.: Deep atmospheric response to the spring Kuroshio over the East China Sea, Journal of Climate, 24,
815 4959–4972, 2011.